Simultaneous Position and Orientation Estimation for Visible Light Systems With Multiple LEDs and Multiple PDs

Shengqiang Shen, Shiyin Li, and Heidi Steendam, *Senior Member, IEEE*

***Abstract*— Visible light communication (VLC) is seen as a supplement for fifth-generation (5G) wireless communication in short-range high data rate communication applications [1]. A reliable VLC system relies on an accurate estimate of the position and orientation of the receiver, which corresponds to the six-dimensional positioning problem mentioned in [2]. In this paper, we investigate the simultaneous position and orientation estimation (SPO) problem using received signal strength (RSS), for a visible light system containing multiple LEDs and multiple photodiodes (PDs) (MLMP). Although in general, the position and orientation of the receiver can be represented by a vector and a rotation matrix, respectively, the constraints imposed by the rotation matrix make the numerical optimization in the estimation process cumbersome, e.g, the commonly used constrained optimization method is often very complex and non-robust. Therefore, in this paper, we design two SPO algorithms using the principle of optimization on manifolds, which alleviates the constraints from the rotation matrix. In addition, we propose an initialization algorithm, based on the direct linear transformation (DLT) principle, to obtain an initial estimate in closed-form for the iterative algorithms. To evaluate the performance of the proposed RSS-based SPO algorithms, we derive the Cramer-Rao bound (CRB). In particular, the orientation error component of the CRB corresponds to the intrinsic CRB or the CRB on manifolds, which measures the error in the estimated rotation matrix in a physically meaningful way. Finally, computer simulations show an asymptotic tightness between the performance of the proposed algorithms and the theoretical lower bound, demonstrating the effectiveness of the proposed solutions.**

***Index Terms*— Visible light system, multiple LEDs and multiple PDs, simultaneous position and orientation estimation, Cramér-Rao bound, optimization on manifolds, interior point method.**

Manuscript received October 1, 2019; revised January 15, 2020; accepted February 17, 2020. Date of publication June 8, 2020; date of current version August 20, 2020. This work was supported in part by the EOS from Belgian Research Councils FWO and FNRS under Grant 30452698 and in part by the Flemish Government (AI Research Program). The work of Shengqiang Shen was supported by the Program of China Scholarship Council under Grant 201706420013. The work of Shiyin Li was supported in part by the National Natural Science Foundation of China under Grant 61771474. *(Corresponding author: Shengqiang Shen.)*

Shengqiang Shen is with Telecommunications and Information Processing Department, Ghent University/IMEC, 9000 Ghent, Belgium, and also with the School of Information and Control Engineering, China University of Mining and Technology, Xuzhou 221116, China (e-mail: shengqiang.shen@ugent.be).

Shiyin Li is with the School of Information and Control Engineering, China University of Mining and Technology, Xuzhou 221116, China (e-mail: lishiyin@cumt.edu.cn).

Heidi Steendam is with Telecommunications and Information Processing Department, Ghent University/IMEC, 9000 Ghent, Belgium (e-mail: Heidi.Steendam@ugent.be).

Color versions of one or more of the figures in this article are available online at http://ieeexplore.ieee.org.

Digital Object Identifier 10.1109/JSAC.2020.3000805

I. Introduction

WHITE LEDs, that are gradually becoming the primary source of light for indoor illumination, can be modulated at frequencies up to several MHz. Consequently, white LEDs can be used for wireless communication, making it possible to achieve high rate communications with low cost, low power consumption, and long lifetime [3]. In addition, visible light is environmentally friendly compared to RF solutions. Electromagnetically sensitive environments, including hospitals and aircrafts, are potential applications. Moreover, due to the dominance of the directional propagation of line-of-sight links (LOS), the visible light channel can be modeled as time invariant [4]. Because of all of these merits, visible light communication (VLC) is seen as a supplement for fifth-generation (5G) wireless communication in short-range high data rate communication applications [1]. However, the visible light channel is largely sensitive to the distance and angle with respect to the transmitter. Therefore, a reliable VLC system requires an accurate estimate of the receiver's position and/or orientation.

VLC-based positioning or visible light positioning (VLP) has been considered in many works [5]. However, research on the orientation of the receiver is limited. Most works on VLP restrict their attention to the special case where the orientation of the receiver is parallel to the transmitter or the ceiling, and some works [6]–[11] consider the performance of the VLP system when the receiver is tilted. In [6], a method to compensate for the RSS changes caused by the tilted orientation is proposed, and the conclusion is that if the compensation is applied, the tilting only results in a slight degradation of the performance, while [8] takes advantage of angular diversity provided by the tilted orientation of the receiver to improve the performance. In [9], the authors analyze the VLP performance for a tilted receiver. However, these papers assume the orientation is known in advance, which is a strong assumption in reality. The effects of unknown orientation were investigated in some papers. In [10], a study of an unknown tilt orientation of the receiver shows that tilting has a significant degradation on the performance. The effect of unknown transmitter and receiver orientations on the channel gain is investigated in [11]. The results show that the effect of an unknown orientation increases with the distance between the transmitter and receiver.

All aforementioned works show that the orientation is important to the visible light system, however, they only investigate the impact of the orientation of the receiver on positioning and do not take into account the orientation estimation. In a reliable visible light system, a simultaneous position and orientation estimation (SPO) algorithm is needed, however, only limited work on SPO is available now. Recently, several SPO algorithms for VLC with a single PD using received signal strength (RSS) have been proposed in [12], [13]. In these papers, a receiver consisting of a single PD is considered, and the orientation of the PD is represented by its normal vector. Although this representation is simple, it has several limitations. Firstly, the normal vector representation is blind to the change in yaw angle, i.e. the representation can not reflect the heading direction. Although this flaw has little impact on the receiver with a single PD in terms of channel gain, the representation fails whenever the heading estimation is required. Secondly, for receivers equipped with multiple PDs or a PD array, the receiver moves and rotates in a rigid manner, and changes in yaw angle of the receiver will affect all PDs that are not at the rotation center. Therefore, instead of representing the orientation using the normal vector, which actually describes the rotation with two degrees of freedom, we consider a more general representation of the orientation, having 3 degrees of freedom, i.e., we use the rotation matrix. The PD array is becoming an increasingly popular topic in both VLC and VLP [14]–[19], because it is able to increase the receiver's FOV and diversity, thereby improving the performance of a visible light system. As the design of efficient SPO algorithms is important for visible light systems with multiple LEDs and multiple PDs (MLMP),[1] we develop in this paper different algorithms to jointly estimate the position and the orientation of the PD array. Further, in this paper, we derive the Cramér-Rao bound (CRB) of the MLMP-based VLP system for unknown but deterministic position and orientation of the receiver. In the literature, several papers are available to incorporate the orientation in the theoretical lower bound. However, either these works consider the case of a known orientation [17], [20]–[22], or they consider the effect of SPO errors for a receiver with a single PD [13], [23], [24]. To the best of our knowledge, the theoretical lower bound that can be used to analytically assess the performance of SPO algorithms for VLP systems with MLMP, was not considered yet.

The main contributions of this paper are as follows:

1) In this paper, we first give the MLMP system model using a rotation matrix to represent the orientation. Because of the constraints imposed by the rotation matrix, classical optimization algorithms operating in Euclidean space are complex. Therefore, we resort to the properties of the rotation matrices, which are elements of the $SO(3)$ matrix Lie group. This $SO(3)$ group is also called the rotation manifold [25], and uses 3 degrees of freedom to describe an orientation. To jointly estimate the rotation matrix and the position in an efficient way, we therefore propose two iterative algorithms using the principle of optimization on manifolds: one based on the Gauss-Newton method (GNM) and the other based on the interior point method (IPM). The latter algorithm further considers the position boundary condition and achieves a better performance in terms of convergence at the cost of computational complexity.

2) In order to provide initial values for the proposed iterative optimization algorithms, we also derive a closed-form approximative solution to the SPO problem using the direct linear transformation (DLT) algorithm combined with the structural features of the angular diversity PD array receiver.

3) To analytically investigate the RSS-based SPO, we derive the associated Cramér-Rao bound (CRB). This CRB simultaneously bounds errors in both the position vector and the rotation matrix. In particular, in order to measure the error in the estimated rotation matrix, the intrinsic CRB on $SO(3)$ is utilized. The performance of the proposed SPO algorithms is assessed using Monte Carlo simulations, and the tightness of the results with the theoretical lower bound is evaluated. Based on the CRB, we also investigate the optimal design of the receiver PD diversity.

The rest of the paper is organized as follows. The model of the MLMP visible light system is described in Section II. The RSS-based SPO algorithms using the optimization on manifolds principle are derived in Section III, together with the expression of the theoretical bound. Subsequently, the closed-form solution using the DLT is discussed in Section IV. Section V gives the numerical results and compares the performance of the proposed methods with the theoretical bound. The optimal design of the PD receiver diversity is evaluated in this section as well. Finally, some concluding remarks are given in Section VI.

II. System Description

A. System Model

In this paper, we consider a system containing N_L LEDs and a VLP receiver containing N_P bare PDs, as shown in Fig. 1. Since all PDs are placed rigidly on the receiver, i.e. all PDs translate and rotate along with the receiver but preserve their relative distances and relative orientations, the coordinates and orientations of the PDs are first defined in the frame of the receiver and then transformed into the frame of the system. In the frame of the receiver, as shown in Fig. 1b, by setting the origin O_r to the centroid of the receiver, the coordinates of the j^{th} PD are specified by a relative distance vector $\mathbf{d}_{j,0} \in \mathbb{R}^{3\times 1}$ to the origin, while the normal of the j^{th} PD is specified by a rotation matrix $\mathbf{R}_{P,j} \in SO(3)$ with respect to a reference orientation $\mathbf{n}_0$, i.e. $\mathbf{n}_{P,j,0} = \mathbf{R}_{P,j}\mathbf{n}_0$, where $\mathbf{R}_{P,j}$ is assumed to be known and fixed. As the reference orientation, we select the normal of the receiver plane, i.e. $\mathbf{n}_0 = [0\ 0\ 1]^{\mathrm{T}}$, as shown in Fig. 1b. In the frame of the system, the position and the orientation of the receiver (the centroid of the receiver) are denoted by $\mathbf{r} \in \mathbb{R}^{3\times 1}$ and $\mathbf{R} \in SO(3)$, respectively, where the receiver's normal $\mathbf{n}$, i.e. the normal of the receiver plane, is expressed by $\mathbf{n} = \mathbf{R}\mathbf{n}_0$, as shown in Fig.1a. The coordinates of the j^{th} PD, denoted by $\mathbf{r}_{P,j}$, are given by $\mathbf{r}_{P,j} = \mathbf{r} + \mathbf{d}_j$, where $\mathbf{d}_j = \mathbf{R}\mathbf{d}_{j,0}$, and the normal of the j^{th} PD is

[1]The multiple LEDs can be compared to the multiple transmitter antennas in a massive MIMO system, and the multiple PDs are the optical counterpart of a receiver antenna array.

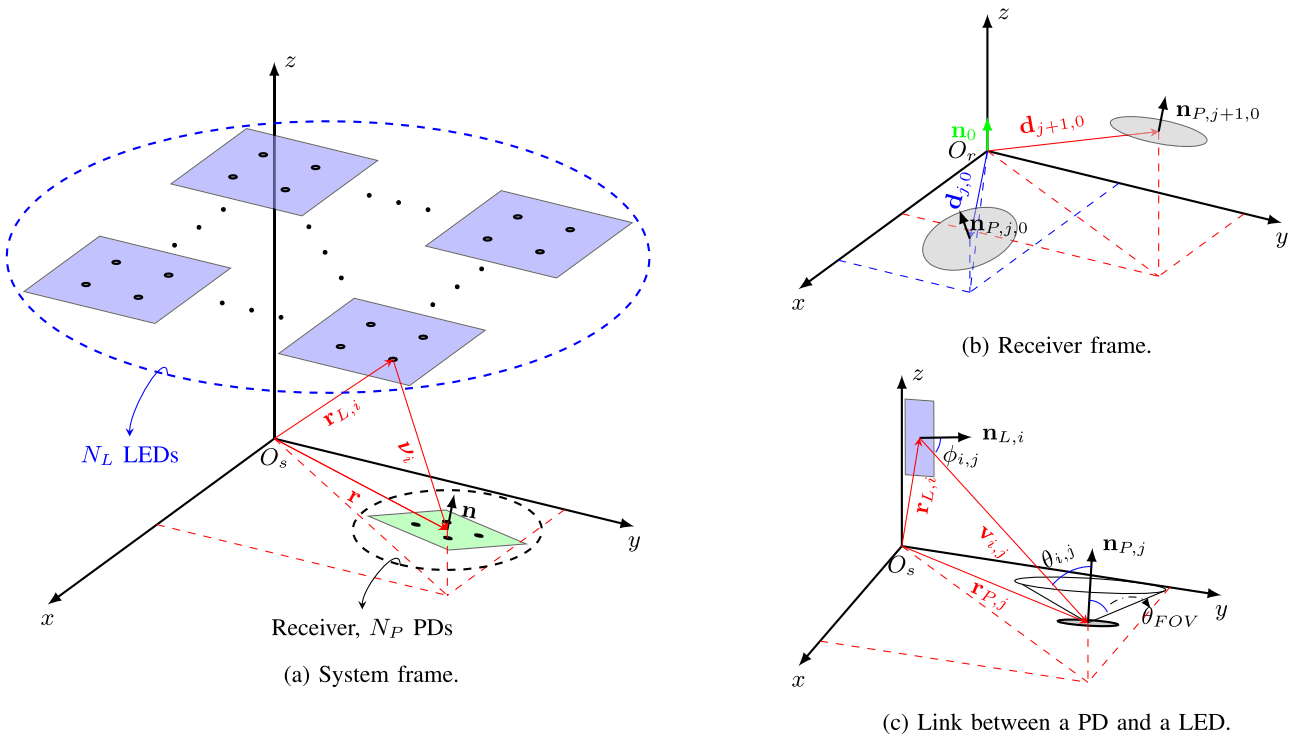

(a) System frame.

(b) Receiver frame.

(c) Link between a PD and a LED.

Fig. 1. System model.

specified by $\mathbf{n}_{P,j} = \mathbf{R}\mathbf{n}_{P,j,0}$. For the transmitter part, it is assumed that the i^{th} LED of the system has coordinates $\mathbf{r}_{L,i} \in \mathbb{R}^{3\times 1}$ and normal $\mathbf{n}_{L,i} \in \mathbb{R}^{3\times 1}$, i.e. the direction in which the LED is radiating. We assume that all LEDs' coordinates, normals, and properties (such as brightness, radiation pattern and modulation settings) are known by the receiver.

B. Channel Gain and Received Power

It is assumed that each PD is able to distinguish between the signals transmitted by the different LEDs. Assuming the vector $\boldsymbol{\nu}_i = \mathbf{r} - \mathbf{r}_{L,i}$ is the vector between the i^{th} LED and the receiver centroid, the incidence vector between the i^{th} LED and the j^{th} PD of the receiver is $\mathbf{v}_{i,j} = \boldsymbol{\nu}_i + \mathbf{d}_j$. Using this definition, we find the distance $v_{i,j}$ between the LED and the PD, the radiation angle $\phi_{i,j}$, i.e. the angle between $\mathbf{v}_{i,j}$ and the normal $\mathbf{n}_{L,i}$ of the LED, and the incidence angle $\theta_{i,j}$, i.e. the angle between the $\mathbf{v}_{i,j}$ and the normal $\mathbf{n}_{P,j}$ of the PD:

$$v_{i,j} = \|\mathbf{v}_{i,j}\|, \tag{1}$$

$$\cos(\phi_{i,j}) = \frac{\mathbf{n}_{L,i}^{\mathrm{T}}\mathbf{v}_{i,j}}{\|\mathbf{v}_{i,j}\|} = \frac{\mathbf{n}_{L,i}^{\mathrm{T}}(\boldsymbol{\nu}_i + \mathbf{d}_j)}{\|\boldsymbol{\nu}_i + \mathbf{d}_j\|}, \tag{2}$$

$$\cos(\theta_{i,j}) = -\frac{\mathbf{n}_{P,j}^{\mathrm{T}}\mathbf{v}_{i,j}}{\|\mathbf{v}_{i,j}\|} = -\frac{\mathbf{n}_{P,j}^{\mathrm{T}}(\boldsymbol{\nu}_i + \mathbf{d}_j)}{\|\boldsymbol{\nu}_i + \mathbf{d}_j\|}. \tag{3}$$

For bare PDs (and upon some constant scaling factor also for PDs with a hemispherical lens), the channel gain corresponding to the LOS component of the i^{th} LED and j^{th} PD is given by [26]:

$$h_{i,j} = \frac{(\gamma+1)A_{R,j}}{2\pi v_{i,j}^2}\cos^{\gamma}(\phi_{i,j})\cos(\theta_{i,j})\,\Pi\left(\frac{\theta_{i,j}}{\theta_{FOV}}\right)\Pi\left(\frac{\phi_{i,j}}{\phi_{FOV}}\right), \tag{4}$$

where $A_{R,j}$ is area of the j^{th} PD (in m^2), θ_{FOV} is the field of view (FOV) of the PD, ϕ_{FOV} is the FOV of the LED, the Lambertian order of the LEDs equals γ, and $\Pi(\cdot)$ is the rectangular function defined as

$$\Pi(x) \triangleq \begin{cases} 1, & |x| \le 1. \\ 0, & |x| > 1. \end{cases} \tag{5}$$

The factor $\Pi(\theta_{i,j}/\theta_{FOV}) \cdot \Pi(\phi_{i,j}/\phi_{FOV})$ in (4) implies that a PD can detect the light only when the LED is within its FOV, and the PD itself is within the FOV of the LED, i.e. when $0 \le \theta_{i,j} \le \theta_{FOV}$ and $0 \le \phi_{i,j} \le \phi_{FOV}$.

Taking into account (1)–(3), (4) can be rewritten as

$$h_{i,j} = K_{i,j}\frac{\left(\mathbf{n}_{L,i}^{\mathrm{T}}(\boldsymbol{\nu}_i + \mathbf{R}\mathbf{d}_{j,0})\right)^{\gamma}}{\|\boldsymbol{\nu}_i + \mathbf{R}\mathbf{d}_{j,0}\|^{\gamma+3}}\left(\mathbf{R}\mathbf{n}_{P,j}\mathbf{n}_0\right)^{\mathrm{T}}(\boldsymbol{\nu}_i + \mathbf{R}\mathbf{d}_{j,0}), \tag{6}$$

where $K_{i,j} = -\frac{(\gamma+1)A_{R,j}\Pi_{i,j}}{2\pi}$ and $\Pi_{i,j} = \Pi(\theta_{i,j}/\theta_{FOV}) \cdot \Pi(\phi_{i,j}/\phi_{FOV})$.

We assume a proper multiplexing protocol is used, e.g. frequency-division multiplexing (FDM) [27], time-division multiplexing (TDM) [28] or color-division multiplexing (CDM) [29], so that each PD is able to separate the signals from the different LEDs. Then the total observation consists of the RSS values from every link between a PD and a LED. Let us define the $N_L N_P \times 1$ vector $\mathbf{y} = \left[\mathbf{y}_1^{\mathrm{T}}, \ldots, \mathbf{y}_{N_P}^{\mathrm{T}}\right]^{\mathrm{T}}$ as the vector of observation, with $\mathbf{y}_j = [y_{1,j}, \ldots, y_{N_L,j}]^{\mathrm{T}}$. Assuming the LOS component dominates the received signal, we obtain

$$\mathbf{y} = \mathbf{h} + \mathbf{w}, \tag{7}$$

where the $N_L N_P \times 1$ vector $\mathbf{h}$ is defined as $\mathbf{h} = \left[\mathbf{h}_1^{\mathrm{T}}, \ldots, \mathbf{h}_{N_P}^{\mathrm{T}}\right]^{\mathrm{T}}$ with $\mathbf{h}_j = R_{p,j}\left[P_{t,1}h_{1,j}, \ldots, P_{t,N_L}h_{N_L,j}\right]^{\mathrm{T}}$,

$P_{t,i}$ is the power transmitted by the i^{th} LED and $R_{p,j}$ is the responsivity of the j^{th} PD. The $N_L N_P \times 1$ vector $\mathbf{w}$ models the shot noise, which is represented by a zero-mean multivariate Gaussian random variable with covariance matrix $\mathbf{\Sigma_w} = \sigma_w^2 \mathbf{I}_{N_L N_P}$. Based on the observation (7) the SPO algorithm needs to jointly estimate the position $\mathbf{r}$ and the orientation $\mathbf{R}$.

III. Estimation Algorithm and Theoretical Bound

In this section, we first show that the SPO problem is a constrained non-linear least squares problem (constrained by the rotation matrix) that can be solved by standard optimization algorithms. However, the resulting algorithms are complex and non-robust. To reduce the complexity and increase the robustness, we then show that by viewing the optimization problem in the $SO(3)$ manifold, the problem reduces to an unconstrained non-linear problem that can be solved using the principle of optimization on manifolds. While in the standard optimization algorithm, the estimated variable and incremental step are in the same Euclidean space, in the optimization algorithm on manifolds, the estimated variable and incremental step are located in different spaces, i.e. the estimated variable in the manifold and the incremental step size in the associated tangent space. We first consider the Gauss-Newton method on manifolds. Its counterpart, i.e. standard Gauss-Newton, is an iterative method that is regularly used for solving non-linear least squares problems. However, the Gauss-Newton method does not always converge properly. Therefore, in order to achieve a proper convergence, we propose an interior point method on manifolds that additionally considers the boundary condition, i.e. the constraint imposed on the position vector. This algorithm is an extension of the standard interior method, which is an effective method to solve non-linear optimization problems that contain an inequality constraint.

Let us define the wanted parameter set $\mathbf{\Theta} = \{\mathbf{r}, \mathbf{R}\}$ and define the log-likelihood function as

$$\begin{aligned}\mathcal{L}(\mathbf{\Theta}; \mathbf{y}) &= \ln p(\mathbf{y}|\mathbf{\Theta}) \\ &= \text{const} - \frac{1}{2}\|\mathbf{y} - \mathbf{h}\|^2_{\mathbf{\Sigma_w}}, \end{aligned} \tag{8}$$

where $\|\mathbf{x}\|^2_{\mathbf{\Sigma}} = \mathbf{x}^{\mathrm{T}}\mathbf{\Sigma}^{-1}\mathbf{x}$ denotes the squared Mahalanobis distance with respect to covariance $\mathbf{\Sigma}$, and $p(\mathbf{y}|\mathbf{\Theta})$ is the conditional probability density function of $\mathbf{y}$ given $\mathbf{\Theta}$, which complies with $\mathbf{y}|\mathbf{\Theta} \sim \mathcal{N}(\mathbf{h}(\mathbf{\Theta}), \mathbf{\Sigma_w})$. The maximum likelihood (ML) estimate of $\mathbf{\Theta}$, i.e. $\hat{\mathbf{\Theta}} = \left\{\hat{\mathbf{r}}, \hat{\mathbf{R}}\right\}$, maximizes the log-likelihood function $\mathcal{L}$:

$$\hat{\mathbf{\Theta}} = \arg\max_{\mathbf{\Theta}} \mathcal{L}. \tag{9}$$

As (9) is a non-linear least squares (NLS) problem, it has no closed-form solution, and has to be solved using an iterative optimization algorithm. Even worse, since $\mathbf{R}$ is a member of $SO(3)$ rather than an arbitrary 3×3 real matrix, $\mathbf{R}$ has to satisfy the following constraints:

$$\mathbf{R}^{\mathrm{T}}\mathbf{R} = \mathbf{R}\mathbf{R}^{\mathrm{T}} = \mathbf{I}, \quad \det(\mathbf{R}) = +1. \tag{10}$$

To solve (9) constrained by (10), we can resort to a constrained non-linear optimization algorithm, which is complex, time consuming and non-robust. However, since $SO(3)$ is an embedded submanifold of $\mathbb{R}^{3\times3}$, we can estimate the parameters in $SO(3)$ using an (iterative) optimization algorithm on manifolds [30]. In each iteration, the algorithm calculates the incremental steps in the tangent space $\mathfrak{so}(3)$ to the manifold $SO(3)$, and then those incremental steps are mapped back on the manifold again to update the steps, which is elaborated in detail in Fig. 2. Since the optimization is iteratively progressed in the manifolds, it relieves the restrictions imposed by the constraints (10), simplifying the optimization process. In Subsection III-A, we adapt Newton's method on $SO(3)$ from [31] to solve the problem at hand, while the interior point method on $SO(3)$ is discussed in Subsection III-B.

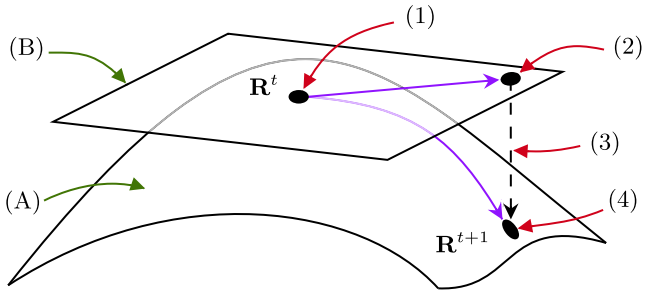

(1) $\mathbf{R}^t$: Current step
(2) Incremential step in $T_{\mathbf{R}^t}SO(3)$
(3) Mapping back to $SO(3)$
(4) $\mathbf{R}^{t+1}$: Updated step
(A) $SO(3)$ manifold
(B) Tangent space at $\mathbf{R}^t$: $T_{\mathbf{R}^t}SO(3) \simeq \mathfrak{so}(3)$

Fig. 2. Optimization on a manifold.

A. Gauss-Newton Method on Manifolds

As in the standard Gauss-Newton optimization, the first step is to find the greatest descent direction to determine the search direction. This search direction $\mathbf{\Delta_\Theta} = \left[\mathbf{\Delta}_{\mathbf{r}}^{\mathrm{T}}, \mathbf{\Delta}_{\mathbf{R}}^{\mathrm{T}}\right]^{\mathrm{T}}$ is given by

$$\mathbf{\Delta_\Theta} = -(\nabla_{\mathbf{\Theta}}\mathbf{h})^{\dagger}(\mathbf{h} - \mathbf{y}), \tag{11}$$

where $(\cdot)^{\dagger}$ denotes the Moore-Penrose pseudoinverse, $\nabla_{\mathbf{\Theta}}\mathbf{h} = [\nabla_{\mathbf{\Theta}}\mathbf{h}_1, \ldots, \nabla_{\mathbf{\Theta}}\mathbf{h}_{N_P}]^{\mathrm{T}} \in \mathbb{R}^{N_L N_P \times 6}$ denotes the Jacobian matrix of $\mathbf{h}$ with respect to $\mathbf{\Theta}$, with $\nabla_{\mathbf{\Theta}}\mathbf{h}_j = R_{p,j}\left[P_{t,1}\nabla_{\mathbf{\Theta}}h_{1,j}, \ldots, P_{t,N_L}\nabla_{\mathbf{\Theta}}h_{N_L,j}\right]^{\mathrm{T}} \in \mathbb{R}^{N_L \times 6}$, and $\nabla_{\mathbf{\Theta}}h_{i,j} = \left[\left(\frac{\partial h_{i,j}}{\partial \mathbf{r}}\right)^{\mathrm{T}}, \left(\frac{\partial h_{i,j}}{\partial \mathbf{R}}\right)^{\mathrm{T}}\right] \in \mathbb{R}^{1\times6}$. The partial derivative $\frac{\partial h_{i,j}}{\partial \mathbf{r}}$ is calculated in Euclidean space, while $\frac{\partial h_{i,j}}{\partial \mathbf{R}}$ is calculated by introducing an infinitesimal perturbation $\exp(\boldsymbol{\omega}_\times)$ [32] as follows,

$$\begin{aligned}&\frac{\partial h_{i,j}}{\partial \mathbf{R}} \\ &= \frac{\partial}{\partial \boldsymbol{\omega}}\bigg|_{\boldsymbol{\omega}=0} \left\{ K_{i,j} \frac{\left(\mathbf{n}_{L,i}^{\mathrm{T}}(\boldsymbol{\nu}_i + \exp(\boldsymbol{\omega}_\times)\mathbf{R}\mathbf{d}_{j,0})\right)^{\gamma}}{\|\boldsymbol{\nu}_i + \exp(\boldsymbol{\omega}_\times)\mathbf{R}\mathbf{d}_{j,0}\|^{\gamma+3}} \right. \\ &\quad \left. \times \left(\exp(\boldsymbol{\omega}_\times)\mathbf{R}\mathbf{R}_{P,j}\mathbf{n}_0\right)^{\mathrm{T}}(\boldsymbol{\nu}_i + \exp(\boldsymbol{\omega}_\times)\mathbf{R}\mathbf{d}_{j,0}) \right\}, \end{aligned} \tag{12}$$

where the infinitesimal perturbation $\exp(\boldsymbol{\omega}_\times) \in SO(3)$ is expressed as

$$\exp(\boldsymbol{\omega}_\times) = \exp\begin{pmatrix} 0 & -\omega_z & \omega_y \\ \omega_z & 0 & -\omega_x \\ -\omega_y & \omega_x & 0 \end{pmatrix}, \tag{13}$$

the operator $(\cdot)_\times$ converts the rotation vector $\boldsymbol{\omega} = [\omega_x\ \omega_y\ \omega_z]^{\mathrm{T}}$ into a skew-symmetric matrix $\boldsymbol{\omega}_\times \in \mathfrak{so}(3)$, and $\exp(\cdot)$ is the matrix exponential function. The partial differential vector of $h_{i,j}$ is then given by

$$\nabla_{\boldsymbol{\Theta}} h_{i,j} = K_{i,j} \cdot \begin{bmatrix} \frac{\gamma\left(\mathbf{n}_{L,i}^{\mathrm{T}}\mathbf{v}_{i,j}\right)^{\gamma-1}\left(\mathbf{n}_{P,j}^{\mathrm{T}}\mathbf{v}_{i,j}\right)}{\|\mathbf{v}_{i,j}\|^{\gamma+3}} \\ \frac{\left(\mathbf{n}_{L,i}^{\mathrm{T}}\mathbf{v}_{i,j}\right)^{\gamma}}{\|\mathbf{v}_{i,j}\|^{\gamma+3}} \\ -\frac{(\gamma+3)\left(\mathbf{n}_{L,i}^{\mathrm{T}}\mathbf{v}_{i,j}\right)^{\gamma}\left(\mathbf{n}_{P,j}^{\mathrm{T}}\mathbf{v}_{i,j}\right)}{\|\mathbf{v}_{i,j}\|^{\gamma+5}} \end{bmatrix}^{\mathrm{T}} \cdot \begin{bmatrix} \mathbf{n}_{L,i}^{\mathrm{T}}, & \mathbf{n}_{L,i}^{\mathrm{T}} \cdot (\mathbf{R}\mathbf{d}_{j,0})_\times^{\mathrm{T}} \\ \mathbf{n}_{P,j}^{\mathrm{T}}, & \boldsymbol{\nu}_i^{\mathrm{T}} \cdot (\mathbf{R}\mathbf{n}_0)_\times^{\mathrm{T}} \\ \mathbf{v}_{i,j}^{\mathrm{T}}, & \boldsymbol{\nu}_i^{\mathrm{T}} \cdot (\mathbf{R}\mathbf{d}_{j,0})_\times^{\mathrm{T}} \end{bmatrix}. \tag{14}$$

In contrast to the standard Gauss-Newton algorithm, the update step for the algorithm on manifolds is given by

$$\mathbf{r}^{t+1} = \mathbf{r}^t + \alpha\boldsymbol{\Delta}_{\mathbf{r}},\ \mathbf{R}^{t+1} = \exp\left((\alpha\boldsymbol{\Delta}_{\mathbf{R}})_\times\right)\mathbf{R}^t, \tag{15}$$

where α is the step size, and $\exp(\cdot)$ maps $(\alpha\boldsymbol{\Delta}_{\mathbf{R}})_\times$ – an element in $\mathfrak{so}(3)$ – back into $\exp\left((\alpha\boldsymbol{\Delta}_{\mathbf{R}})_\times\right)$ – an element in $SO(3)$, i.e. step (3) in Fig. 2.

B. Interior Point Method on Manifolds

In our experiments, we found that the Gauss-Newton algorithm not always converges properly, especially when the SNR is low or the number of observations is small. In these situation, it often happens that a position is found that is outside of the room with the LEDs and reciver. To avoid such outliers and improve the convergence of the algorithm, in the following we design an interior point method on manifolds that takes into account a boundary condition, i.e. the position of the receiver is confined within a target area (the room), which is expressed as $\mathbf{0} \leq \mathbf{r} \leq \mathbf{b}$, where the position $\mathbf{r}$ of the receiver is confined within the bounds of the room given by the coordinates $\mathbf{0}$ and $\mathbf{b}$. As the bounds $\mathbf{0} \leq \mathbf{r} \leq \mathbf{b}$ are hard to implement in a practical optimization algorithm, due to the discontinuity of the equality sign, the interior point method replaces the strict inequality by a barrier function $-\mu\sum_{i=1}^{6}\log([\mathbf{s}]_i)$, where $\mathbf{s}$ is a slack variable vector and μ is the barrier parameter, and $[\cdot]_i$ is defined as the operator that returns the i^{th} element when the operand is a vector and it returns the i^{th} row as a row vector when the operand is a matrix. Forcing $\mathbf{s}$ to be strictly positive is equivalent to $\mathbf{0} \leq \mathbf{r} \leq \mathbf{b}$. This barrier function is added as a penalty function to our objective function (9) to enforce the boundary condition:

$$\begin{aligned} \hat{\boldsymbol{\Theta}} = \ & \arg\min_{\boldsymbol{\Theta}} \left\{ -\mathcal{L} - \mu\sum_{i=1}^{6}\log([\mathbf{s}]_i) \right\}, \\ & s.t.\ \mathbf{c} - \mathbf{s} = 0 \end{aligned} \tag{16}$$

where $\mathbf{c}^{\mathrm{T}} = \left[\mathbf{r}^{\mathrm{T}}, (\mathbf{b}-\mathbf{r})^{\mathrm{T}}\right]$ is the rearranged inequality vector. The interior point method consists of finding (approximate) solutions of (16) for a sequence of positive $\{\mu\}$ that converges to zero. In the first steps, the barrier parameter μ is taken strictly positive to keep the algorithm within the feasible region, whereas in later steps, the barrier parameter converges to zero to better resemble the condition $\mathbf{0} \leq \mathbf{r} \leq \mathbf{b}$. For each μ, the interior point method finds the solution to the Karush-Kuhn-Tucker (KKT) conditions for (16) using Newton's method. As such, the interior point method is a two-level iteration algorithm, where the outer iteration decays μ gradually and the inner iteration updates iteratively the state (comprised of the parameter set $\boldsymbol{\Theta}$, the Lagrange multiplier $\mathbf{z}$ of $\mathbf{c}$, and the slack variable vector $\mathbf{s}$) for a given μ. To determine the search direction $(\boldsymbol{\Delta}_{\boldsymbol{\Theta}}, \boldsymbol{\Delta}_{\mathbf{z}}, \boldsymbol{\Delta}_{\mathbf{s}})$ for the inner iteration, the algorithm finds the solution to the symmetric primal-dual system [33], which is given by

$$\begin{bmatrix} -\nabla^2_{\boldsymbol{\Theta}\boldsymbol{\Theta}}\mathcal{L}(\boldsymbol{\Theta}) & \mathbf{A}^{\mathrm{T}} \\ \mathbf{A} & -\mathbf{Z}^{-1}\mathbf{S} \end{bmatrix} \cdot \begin{bmatrix} \boldsymbol{\Delta}_{\boldsymbol{\Theta}} \\ -\boldsymbol{\Delta}_{\mathbf{z}} \end{bmatrix} = \begin{bmatrix} \mathbf{A}^{\mathrm{T}}\mathbf{z} + \nabla_{\boldsymbol{\Theta}}\mathcal{L}(\boldsymbol{\Theta}) \\ \mu\mathbf{Z}^{-1}\mathbf{1} - \mathbf{c} \end{bmatrix}, \tag{17a}$$

$$\boldsymbol{\Delta}_{\mathbf{s}} = \mathbf{Z}^{-1}\left(\mu\mathbf{1} - \mathbf{Z}\mathbf{s} - \mathbf{S}\boldsymbol{\Delta}_{\mathbf{z}}\right), \tag{17b}$$

where $\mathbf{1}$ is the all-ones vector, the diagonal matrices $\mathbf{Z}$ and $\mathbf{S}$ are given by $\mathbf{Z} = \mathrm{diag}(\mathbf{z})$, $\mathbf{S} = \mathrm{diag}(\mathbf{s})$, respectively, and

$$\mathbf{A} = \begin{bmatrix} \mathbf{I}_{3\times3} & \mathbf{0}_{3\times3} \\ -\mathbf{I}_{3\times3} & \mathbf{0}_{3\times3} \end{bmatrix} \tag{18}$$

is the Jacobian matrix of $\mathbf{c}$ with respect to $\boldsymbol{\Theta}$. Since in the Hessian matrix in (17a), the analytical derivation of $\nabla^2_{\boldsymbol{\Theta}\boldsymbol{\Theta}}\mathcal{L}(\boldsymbol{\Theta})$ is cumbersome, in the following it is approximated by $\nabla^2_{\boldsymbol{\Theta}\boldsymbol{\Theta}}\mathcal{L}(\boldsymbol{\Theta}) \approx (\nabla_{\boldsymbol{\Theta}}\mathbf{h})^{\mathrm{T}}(\nabla_{\boldsymbol{\Theta}}\mathbf{h})$. Note that the same expression can be found in the Moore-Penrose pseudoinverse, used in the Gauss-Newton algorithm.

The solution of (17) defines the search direction for the inner iteration, while the step length is determined by

$$\begin{aligned} \alpha^{\max}_{\mathbf{s}} = \ & \max\{\alpha \in (0,1] : \mathbf{s} + \alpha\boldsymbol{\Delta}_{\mathbf{s}} \geq (1-\tau)\,\mathbf{s}, \\ & \alpha\|\boldsymbol{\Delta}_{\mathbf{R}}\| \leq (1-\tau)\,\pi\}, \end{aligned} \tag{19a}$$

$$\alpha^{\max}_{\mathbf{z}} = \max\{\alpha \in (0,1] : \mathbf{z} + \alpha\boldsymbol{\Delta}_{\mathbf{z}} \geq (1-\tau)\,\mathbf{z}\}. \tag{19b}$$

The constraint, $\alpha\|\boldsymbol{\Delta}_{\mathbf{R}}\| \leq (1-\tau)\,\pi$, in the formula of $\alpha^{\max}_{\mathbf{s}}$ prevents the absolute value of the incremental step for $\mathbf{R}$ from being larger than π, which arises from the fact that the matrix exponential function that converts the incremental step back in the manifold is a periodic function with a period of 2π. As a result, the update step for the interior point algorithm on manifolds is given by

$$\mathbf{r}^{t+1} = \mathbf{r}^t + \alpha_{\mathbf{s}}\boldsymbol{\Delta}_{\mathbf{r}},\ \mathbf{R}^{t+1} = \exp\left((\alpha_{\mathbf{s}}\boldsymbol{\Delta}_{\mathbf{R}})_\times\right)\mathbf{R}^t, \tag{20a}$$

$$\mathbf{s}^{t+1} = \mathbf{s}^t + \alpha_{\mathbf{s}}\boldsymbol{\Delta}_{\mathbf{s}},\ \ \mathbf{z}^{t+1} = \mathbf{z}^t + \alpha_{\mathbf{z}}\boldsymbol{\Delta}_{\mathbf{z}}. \tag{20b}$$

The merit function measuring the quality of an updated state is given in terms of the barrier function (16) by

$$m_\iota(\boldsymbol{\Theta}, \mathbf{s}) = -\mathcal{L}(\boldsymbol{\Theta}) - \mu\sum_{i=1}^{6}\log([\mathbf{s}]_i) + \iota\|\mathbf{c} - \mathbf{s}\|_1, \tag{21}$$

where ι is the penalty parameter that determines the weight that we assign to constraint satisfaction relative to the minimization of the objective. The error function (reflecting the maximum residual error in the KKT conditions), which indicates whether a local minimum solution is achieved, is calculated by [33]

$$\epsilon = \max\left\{\|\nabla_{\mathbf{\Theta}}\mathcal{L}\left(\mathbf{\Theta}\right)+\mathbf{A}^{\mathrm{T}}\mathbf{z}\|, \|\mathbf{S}\mathbf{z}-\mu\mathbf{1}\|, \|\mathbf{c}-\mathbf{s}\|\right\}. \quad (22)$$

An overview of the proposed interior point method on the $SO(3)$ manifold is shown in Algorithm 1, where ϵ_{TOL} is the tolerance that specifies the required accuracy of the computed solution, μ is initialized by a large positive number and decreases iteratively with a decay rate of σ, and τ could be set to a typical value of $\tau = 0.995$ [33].

Algorithm 1 Algorithm for IPM on the $SO(3)$ Manifold

Input: $\mathbf{0} \leq \mathbf{r}^0 \leq \mathbf{b}$, $\mathbf{R}^0 \in SO(3)$
Output: $\mathbf{\Theta}$
Initialisation: Select $\mu > 0, \tau \in (0,1), \sigma \in (0,1), \epsilon_{\mathrm{TOL}}$, set $t = 0$
Compute $\mathbf{z}^0, \mathbf{s}^0$
LOOP Process
for $i = 1$ to maxiterations$_o$ **do**
  for $j = 1$ to maxiterations$_i$ **do**
    Compute $\mathbf{\Delta}_{\mathbf{\Theta}}, \mathbf{\Delta}_{\mathbf{z}}, \mathbf{\Delta}_{\mathbf{s}}$ from (17)
    Compute $\alpha_{\mathbf{s}}^{\max}, \alpha_{\mathbf{z}}^{\max}$ using (19)
    Compute $\alpha_{\mathbf{s}} \in (0, \alpha_{\mathbf{s}}^{\max}], \alpha_{\mathbf{z}} \in (0, \alpha_{\mathbf{z}}^{\max}]$ such that (21) decreases
    Update $\mathbf{\Theta}, \mathbf{s}, \mathbf{z}$ using (20)
    Compute ϵ from (22)
    if $\epsilon \leq \epsilon_{\mathrm{TOL}}$ **then**
      break
    end if
  end for
  Set $\mu = \sigma\mu$
end for
return $\mathbf{\Theta}$

C. Convergence and Complexity Analysis

Besides the performance of the proposed methods, which will be discussed in Section V, we also want to discuss the convergence and complexity of the algorithms. First we discuss the convergence. In the Gauss-Newton method, the convergence is determined by the properties of the Jacobian matrix $\nabla_{\mathbf{\Theta}}\mathbf{h}$. Assuming the dimension of the observation vector is not less than the number of unknown parameters, the Jacobian matrix is full-row-rank, implying $\nabla_{\mathbf{\Theta}}\mathbf{h}$ is invertible. Further, since $\left(\left(\nabla_{\mathbf{\Theta}}\mathcal{L}\right)^{\mathrm{T}} \cdot \Delta_{\mathbf{\Theta}}\right) < 0$ holds for any non-critical point, the sequence $\{\Delta_{\mathbf{\Theta}}\}$ of incremental steps towards the optimal $\mathbf{\Theta}$ is a gradient-related sequence, whose accumulation point $\Delta_{\mathbf{\Theta}}^{\bullet}$ is a critical point according to the convergence of line-search methods. As a consequence, in the neighborhood of $\Delta_{\mathbf{\Theta}}^{\bullet}$, the convergence rates of the Gauss-Newton method is superlinear [30]. On the other hand, in the interior point method, the convergence rate is determined by the properties of the Hessian matrix of the objective function in (16) and its approximation. In case the difference between the actual and approximated Hessian matrices becomes sufficiently small at the critical point, the optimization in the inner iteration will converge superlinearly [30]. In the situation at hand, the approximated Hessian matrix differs from the actual one by a symmetric matrix that equals zero at the critical point, implying the inner iterations converges superlinearly. By reducing the barrier parameter μ at an appropriate rate [34], the convergence of the combination of inner and outer iterations, i.e., the interior point method as a whole, also is superlinear. Hence, both proposed algorithms will show superlinear convergence rates.

Next, we discuss the complexity. In the Gauss-Newton method, the complexity during each iteration is dominated by the computation of the Moore-Penrose pesudoinverse of $\nabla_{\mathbf{\Theta}}\mathbf{h}$, which is a $N_L N_L \times 6$ matrix. As a consequence, the Gauss-Newton method has a complexity of $\mathcal{O}\left(\left(N_L N_P\right)^2\right)$ flops per iteration [35]. On the other hand, the complexity of the interior point method is dominated by the matrix inversion required to solve (17a) in each inner iteration. Therefore, the interior point method has a complexity of $\mathcal{O}\left(\left(N_L N_P\right)^3\right)$ flops per iteration [35]. Hence, it is clear that the complexity of the interior point method is higher than that of the Gauss-Newton method.

D. The Theoretical Lower Bound

We first define the measure of the estimation error in the estimated position and orientation. The estimation error in position is straightforwardly measured by the relative distance between $\hat{\mathbf{r}}$ and $\mathbf{r}$, i.e. $\mathbf{r}_\epsilon = \hat{\mathbf{r}} - \mathbf{r}$, while the estimation error in orientation is measured by the rotation error projected onto the Lie algebra, i.e. $\left(\mathbf{u}_\epsilon\right)_\times = \log\left(\mathbf{R}_\epsilon\right)$, where the matrix logarithmic function $\log(\cdot)$ maps from $SO(3)$ into $\mathfrak{so}(3)$, and

$$\mathbf{R}_\epsilon = \mathbf{R}\hat{\mathbf{R}}^{\mathrm{T}} \in SO(3) \quad (23)$$

is the error rotation matrix that physically measures how much $\hat{\mathbf{R}}$ must rotate to reach $\mathbf{R}$. According to Euler's rotation theorem [36], $\mathbf{u}_\epsilon$ is physically the axis-angle presentation of the rotation matrix $\mathbf{R}_\epsilon$, implying $\mathbf{u}_\epsilon$ could be calculated more conveniently by

$$\mathbf{u}_\epsilon = \frac{\theta_\epsilon}{2\sin\theta_\epsilon}\begin{bmatrix}[\mathbf{R}_\epsilon]_{3,2} - [\mathbf{R}_\epsilon]_{2,3} \\ [\mathbf{R}_\epsilon]_{1,3} - [\mathbf{R}_\epsilon]_{3,1} \\ [\mathbf{R}_\epsilon]_{2,1} - [\mathbf{R}_\epsilon]_{1,2}\end{bmatrix}, \quad (24)$$

where $\theta_\epsilon = \arccos\left(\frac{\mathrm{tr}(\mathbf{R}_\epsilon)-1}{2}\right)$ represents the angle component of $\mathbf{u}_\epsilon$ physically. Here, we define a unified estimation error vector $\mathbf{g}_\epsilon$ measuring the overall error, with $\mathbf{g}_\epsilon = [\mathbf{r}_\epsilon^{\mathrm{T}}, \xi\mathbf{u}_\epsilon^{\mathrm{T}}]^{\mathrm{T}}$, where $\xi > 0$ reflects the scale order on the orientation error compared to the position error. Then using the CRB for vector parameter transformation [37], the error covariance matrix of $\mathbf{g}_\epsilon$ is lower bounded by

$$E\{\mathbf{g}_\epsilon\mathbf{g}_\epsilon^{\mathrm{T}}\} \succeq \mathrm{diag}\left(\left[\mathbf{1}^{\mathrm{T}}, \xi\mathbf{1}^{\mathrm{T}}\right]\right)\mathbf{J}^{-1}\mathrm{diag}\left(\left[\mathbf{1}^{\mathrm{T}}, \xi\mathbf{1}^{\mathrm{T}}\right]\right), \quad (25)$$

where

$$\mathbf{J} = \frac{1}{\sigma_w^2}\left(\nabla_{\mathbf{\Theta}}\mathbf{h}\right)^{\mathrm{T}}\left(\nabla_{\mathbf{\Theta}}\mathbf{h}\right) \quad (26)$$

is the Fisher information matrix. Taking into account [38], it follows that the orientation associated component of (25) is actually the intrinsic CRB on $SO(3)$. To get the lower bound on the error covariance matrix of $\mathbf{r}_\epsilon$, we first rewrite the Fisher information matrix as a partitioned matrix,

$$\mathbf{J} = \begin{bmatrix} \mathbf{J}(\mathbf{r}_\epsilon, \mathbf{r}_\epsilon) & \mathbf{J}(\mathbf{r}_\epsilon, \mathbf{u}_\epsilon) \\ \mathbf{J}(\mathbf{u}_\epsilon, \mathbf{r}_\epsilon) & \mathbf{J}(\mathbf{u}_\epsilon, \mathbf{u}_\epsilon) \end{bmatrix}. \tag{27}$$

Consequently,

$$E\{\mathbf{r}_\epsilon \mathbf{r}_\epsilon^{\mathrm{T}}\} \succeq \left[\mathbf{J}(\mathbf{r}_\epsilon, \mathbf{r}_\epsilon) - \mathbf{J}(\mathbf{r}_\epsilon, \mathbf{u}_\epsilon)\mathbf{J}^{-1}(\mathbf{u}_\epsilon, \mathbf{u}_\epsilon)\mathbf{J}(\mathbf{u}_\epsilon, \mathbf{r}_\epsilon)\right]^{-1}. \tag{28}$$

Similarly, the error covariance matrix of $\mathbf{u}_\epsilon$ is lower bounded by

$$E\{\mathbf{u}_\epsilon \mathbf{u}_\epsilon^{\mathrm{T}}\} \succeq \left[\mathbf{J}(\mathbf{u}_\epsilon, \mathbf{u}_\epsilon) - \mathbf{J}(\mathbf{u}_\epsilon, \mathbf{r}_\epsilon)\mathbf{J}^{-1}(\mathbf{r}_\epsilon, \mathbf{r}_\epsilon)\mathbf{J}(\mathbf{r}_\epsilon, \mathbf{u}_\epsilon)\right]^{-1}. \tag{29}$$

IV. Initial Coarse Estimation

The algorithms given in the previous section are iterative methods, and a proper initialization is required for convergence. To this end, we propose in this section an initialization algorithm. In the following, we assume that all LEDs are installed at the ceiling and an angular diversity receiver is considered. This receiver type, which is considered in several works [19], [39]–[41], consists of multiple PDs orientated symmetrically at different directions to achieve a better angular diversity. More specifically, $N_{P,s}$ PDs are placed symmetrically around the center of the receiver, and are tilted away from the center of the receiver, as shown in Fig. 3. Let the angle between the normal of the receiver and the normal of a PD be θ_P. Using the axis-angle representation, the normal of the j^{th} PD is specified by $\mathbf{n}_{P,j,0} = \exp\left((\theta_P \mathbf{z}_{P,j})_\times\right)\mathbf{n}_0$, where $\mathbf{z}_{P,j} = [\cos(j2\pi/N_{P,s}), \sin(j2\pi/N_{P,s}), 0]^{\mathrm{T}}$. An additional PD placed right above the center of the receiver has normal $\mathbf{n}_0$. The relative distance vector $\mathbf{d}_{j,0}$ that specifies the position of j^{th} PD to the center of the receiver is given by $\mathbf{d}_{j,0} = d_j \mathbf{n}_{P,j,0}$, i.e. $\mathbf{d}_{j,0}$ is parallel to $\mathbf{n}_{P,j,0}$. In the following, we will show that the problem of position and orientation estimation can be converted into a plane-based pose estimation problem, by properly selecting a set of points at the ceiling that correspond to the intersections of the normals $\mathbf{n}_{P,j,0}$ on the virtual image plane, i.e., the plane in the frame of the receiver containing all points having amplitude 1 in the z-direction. This plane-based pose estimation problem can easily be solved using the direct linear transformation (DLT) method from computer vision. As in this method, the points at the ceiling must be known, we design a method to estimate these points.

First, let us define two planes: P' denotes the plane of ceiling, while P is the virtual image plane containing the point $\mathbf{q}_j = \mathbf{n}_{P,j,0} / [\mathbf{n}_{P,j,0}]_3$.[2] Let $\mathbf{q}'_j$ represent the intersection point of the plane P' with the line starting from the center $\mathbf{r}$ of the receiver and radiating in the direction $\mathbf{n}_{P,j}$. Assuming the intersection points $\mathbf{q}'_j$ are known (the estimation of $\mathbf{q}'_j$ is deferred to the end of this section), then the problem of finding the closed-form SPO solution is converted into a plane-based pose estimation problem[3] as shown in Fig. 4. With at least four $(\mathbf{q}'_j, \mathbf{q}_j)$, the position vector and rotation matrix can be estimated using the direct linear transformation (DLT) method [42], which is a commonly used method for the estimation of the relative pose between a plane and a camera, based on projections of sets of coplanar features in computer vision. The solution of the DLT is given by

$$\begin{cases} \hat{\mathbf{R}} = \begin{bmatrix} \hat{\mathbf{T}}^{\mathrm{T}} \\ \left[\hat{\mathbf{T}}^{\mathrm{T}}\right]_1 \times \left[\hat{\mathbf{T}}^{\mathrm{T}}\right]_2 \end{bmatrix}, \\ \hat{\mathbf{r}} = -\hat{\mathbf{R}}\mathbf{M} \begin{bmatrix} 0 \\ 0 \\ \lambda \end{bmatrix} + \mathrm{diag}\left([0,0,1]^{\mathrm{T}}\right)\mathbf{b}, \end{cases} \tag{30}$$

where $\mathbf{b}$ is the boundary condition (see Subsection III-B), $\lambda = \frac{\mathrm{tr}(\hat{\mathbf{T}}^{\mathrm{T}}\mathbf{M})}{\mathrm{tr}(\hat{\mathbf{M}}^{\mathrm{T}}\mathbf{M})}$, $\mathbf{M}$ is given by

$$[[\mathbf{M}]_1, [\mathbf{M}]_2, [\mathbf{M}]_3]^{\mathrm{T}} = \mathbf{m}, \tag{31}$$

with $\mathbf{m}$ the last column of $\mathbf{V}_\mathbf{Q}$ that comes from the Singular Value Decomposition (SVD) of $\mathbf{Q} = \mathbf{U}_\mathbf{Q}\mathbf{\Lambda}_\mathbf{Q}\mathbf{V}_\mathbf{Q}^{\mathrm{T}}$, where the diagonal elements of $\mathbf{\Lambda}_\mathbf{Q}$ are arranged in descending order, and the matrix $\mathbf{Q}^{\mathrm{T}} = [\mathbf{Q}_1^{\mathrm{T}}, \ldots, \mathbf{Q}_N^{\mathrm{T}}]$, where $\mathbf{Q}_i$ is defined as

$$\mathbf{Q}_i = \begin{bmatrix} \mathbf{0}_{3\times1}, & -\mathbf{q}'^{\mathrm{T}}_i, & [\mathbf{q}_i]_2 \mathbf{q}'^{\mathrm{T}}_i \\ -\mathbf{q}'^{\mathrm{T}}_i, & \mathbf{0}_{3\times1}, & -[\mathbf{q}_i]_1 \mathbf{q}'^{\mathrm{T}}_i \end{bmatrix}. \tag{32}$$

The matrix $\hat{\mathbf{T}} \in \mathbb{R}^{3\times2}$ in (30) is given by $\hat{\mathbf{T}} = \mathbf{U}_\mathbf{T}\mathbf{V}_\mathbf{T}^{\mathrm{T}}$, where $\mathbf{U}_\mathbf{T}$ and $\mathbf{V}_\mathbf{T}$ come from the thin SVD of $\left[[\mathbf{M}]^1, [\mathbf{M}]^2\right] = \mathbf{U}_\mathbf{T}\mathbf{\Lambda}_\mathbf{T}\mathbf{V}_\mathbf{T}^{\mathrm{T}}$, where the operator $[\cdot]^i$ returns the i^{th} column of a matrix as a column vector. Since the above algorithm does not make any assumption about the visibility of either side of the plane P', another potential estimate exists, i.e., the mirror

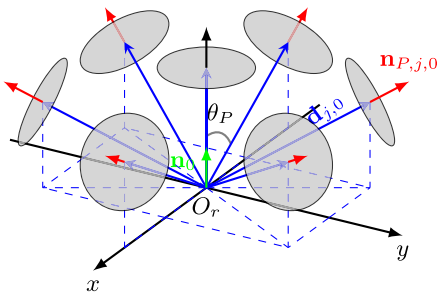

Fig. 3. Angular diversity receiver with $N_{P,s} = 6$.

[2]Taking into account that the plane P contains all points with $[\mathbf{x}]_3 = 1$, i.e., having amplitude 1 in the z-direction, then $\mathbf{q}_j$ is the intersection point of P with the line starting in O_r and radiating in the direction $\mathbf{n}_{P,j,0}$. Since both $\mathbf{q}_j$ and P are defined in the frame of the receiver, they will move and rotate along with the receiver in a rigid way, i.e. $\mathbf{q}_j$ has a fixed location on P.

[3]Because $\mathbf{q}_j$ and P move and rotate along with the receiver in a rigid way, $\mathbf{q}'_j$ is actually the projection of $\mathbf{q}_j$ along $\mathbf{n}_{P,j}$ on P'. However, if we switch the roles of these two points (taking $\mathbf{q}'_j$ as the object and $\mathbf{q}_j$ as the projection), $\mathbf{q}_j$ and $\mathbf{q}'_j$ could be viewed as points in a pinhole camera model where the pinhole is positioned at the receiver center $\mathbf{r}$ and has a focus of unit length. "Object" $\mathbf{q}'_j$ (in the frame of the system) is "projected" onto the virtual image plane as $\mathbf{q}_j$ (represented by homogeneous coordinates in the frame of the receiver).

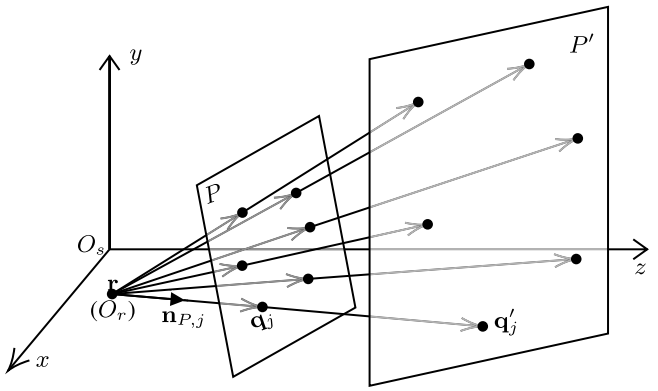

Fig. 4. Plane-based pose estimation problem. P: the virtual image plane, P': the plane of the ceiling.

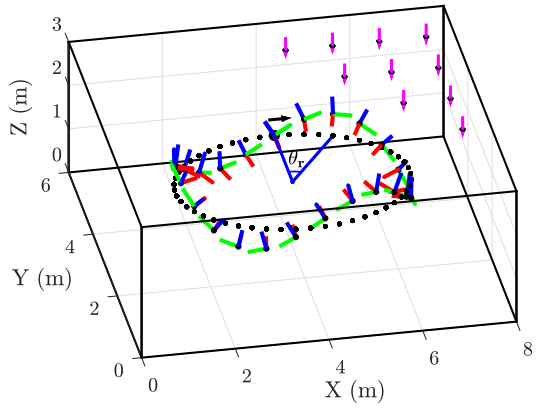

Fig. 5. Simulation setup. The three orthonormal vectors in three different colors at each sample on the path represent the frame of the receiver (shown with $\theta_R = 0°$), where the red, green and blue vector represent the x-axis, y-axis and z-axis, respectively. The pink arrows represent the LEDs (only a fraction of them are shown) on the ceiling. $\theta_\mathbf{r}$ indicates the traveled angle along the dotted ellipse in the XY plane.

symmetry with respect to the plane P', given by

$$\begin{cases} \hat{\mathbf{R}} = \operatorname{diag}\left([-1,-1,1]^{\mathrm{T}}\right) \begin{bmatrix} \hat{\mathbf{T}}^{\mathrm{T}} \\ \left[\hat{\mathbf{T}}^{\mathrm{T}}\right]_1 \times \left[\hat{\mathbf{T}}^{\mathrm{T}}\right]_2 \end{bmatrix}. \\ \hat{\mathbf{r}} = \hat{\mathbf{R}}\mathbf{M} \begin{bmatrix} 0 \\ 0 \\ \lambda \end{bmatrix} + \operatorname{diag}\left([0,0,1]^{\mathrm{T}}\right) \mathbf{b}. \end{cases} \tag{33}$$

From the two possible solutions, the algorithm has to select the solution for which $[\hat{\mathbf{r}}]_3 \leq [\mathbf{b}]_3$, implying that the z coordinate of the estimated position must be smaller than the boundary in the z direction.

The remaining problem is to find a method to estimate the intersection point $\mathbf{q}'_j$. The idea to achieve this is based on the observation that typically the relative distance between PDs within a PD array is very small compared with the distance between the receiver and LEDs. Hence, for each LED we can select the PD within the array that receives the largest power from this LED. Due to the channel characteristics, this selected PD is, in the absence of noise, the one with the smallest incident angle for that LED. Following the idea above, we could find a set of LEDs, for which the j^{th} PD has the smallest incident angle. The spatial average (weighted by associated received power) of the positions of the LEDs within this set can be seen as an approximation to $\mathbf{q}'_j$.

A second initial point, $\{\mathbf{b}/2, \mathbf{I}_3\}$ (the receiver pointing upwards and located at the center the area) is also considered in our paper to ensure that the iterative algorithm converges to the global optimum and to serve as a valid initial point when the DLT algorithm fails, i.e., when less than 4 pairs of $(\mathbf{q}'_j, \mathbf{q}_j)$ are obtained or three out of four of the obtained intersection points $\mathbf{q}'_j$ are collinear [43].

V. Numerical Results

In the evaluation of the estimator and the theoretical lower bound through computer simulations, we consider an 8 m×6 m×3 m area ($\mathbf{b} = [8,6,3]^{\mathrm{T}}$) with $N_L = 48$ LEDs. The LEDs are uniformly distributed over the ceiling, with the number of LEDs in the X direction $N_{L,X} = 8$ and in the Y direction $N_{L,Y} = 6$, i.e., the positions of the LEDs are given

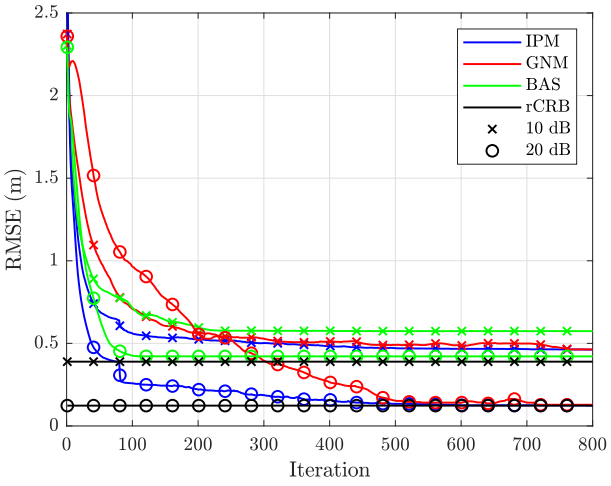

(a)

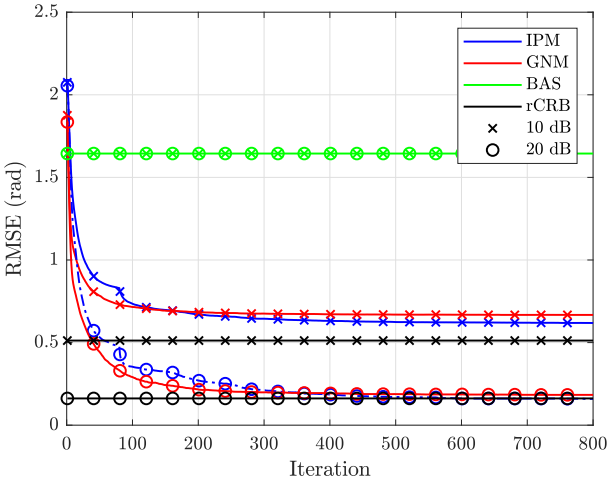

(b)

Fig. 6. RMSE versus iteration for SNR= 10 dB and SNR= 20 dB. (a) Position estimation errors, (b) Orientation estimation errors.

by $\left[\frac{[\mathbf{b}]_1(2i-1)}{2N_{L,X}}, \frac{[\mathbf{b}]_2(2j-1)}{2N_{L,Y}}, [\mathbf{b}]_3\right]^{\mathrm{T}}$, with $i \in \{1,\ldots,N_{L,X}\}$ and $j \in \{1,\ldots,N_{L,Y}\}$. All LEDs are assumed to have a transmit power of $P_t = 1$ W, a Lambertian order $\gamma = 1$, an FOV

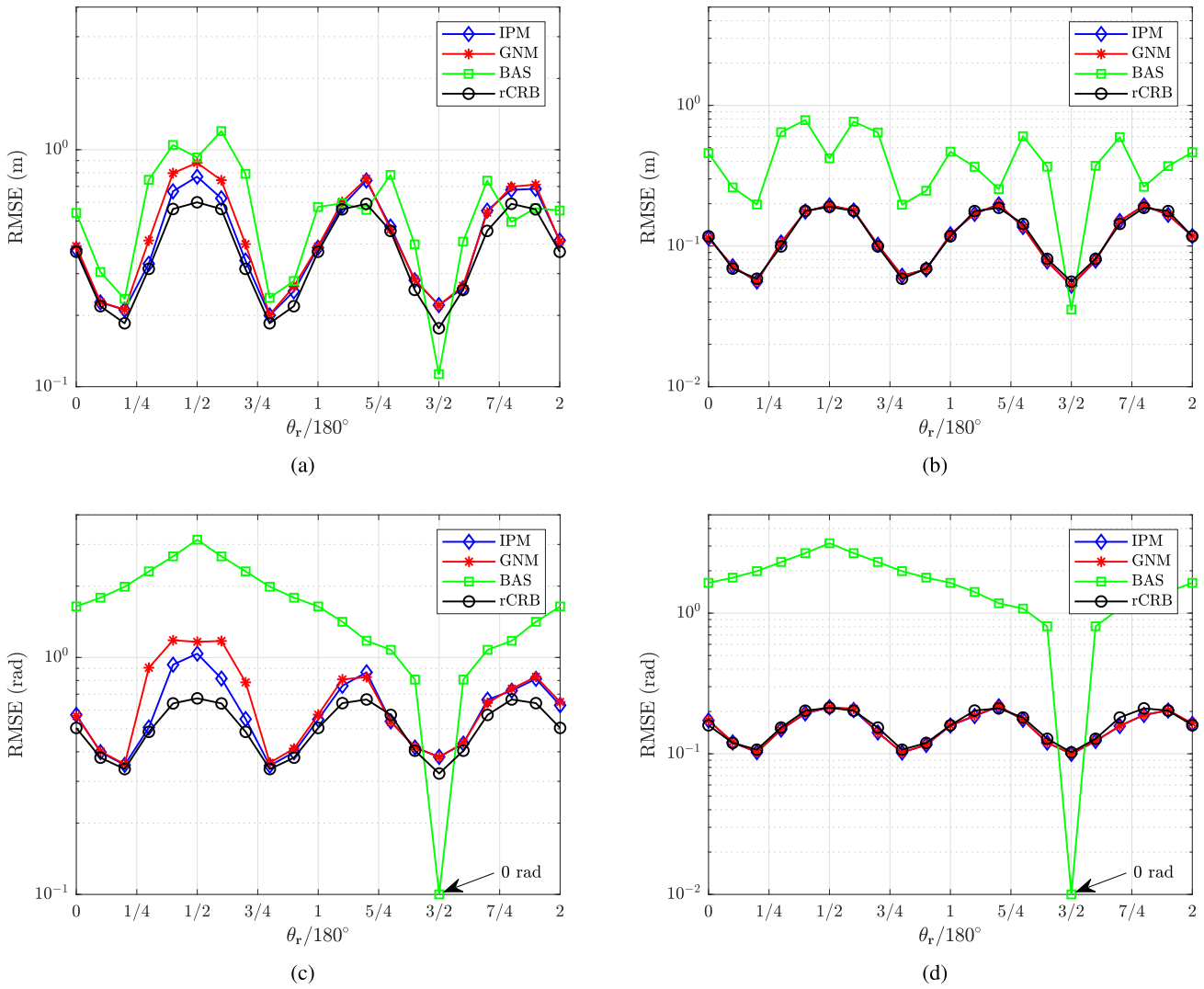

Fig. 7. RMSE of the estimator and the theoretical bound for $\theta_R = 0°$. SNR $= 10$ dB for (a) and (c), SNR $= 20$ dB for (b) and (d). Top row contains position estimation errors ((a) and (b)), while bottom row contains orientation estimation errors ((b) and (d)).

of $\phi_{FOV} = 90°$ and point downwards ($\mathbf{n}_{L,i} = [0, 0, -1]^{\mathrm{T}}$). The receiver consists of seven PDs, with six of them being symmetrically equipped around the centroid and tilted away from the center by $\theta_P = 40°$. All PDs have a relative vector (the distance vector to the centroid) of $\mathbf{d}_{j,0} = d_j \mathbf{n}_{P,j,0}$, with $d_j = 0.02$ m (see Section IV for the expression of $\mathbf{n}_{P,j,0}$). Each PD is assumed to have an FOV of $\theta_{FOV} = 80°$, a unit responsivity $R_p = 1$ and an area of $A_R = \pi r_P^2$ with the radius $r_P = 5 \times 10^{-3}$ m. The above parameter settings for the physical properties of the LEDs and the PDs are similar to the ones used in [44]. To evaluate the performance of the estimators, we consider the path shown in Fig. 5. The path has an elliptical pattern in the XY plane and a sinusoidal pattern in the Z direction. The semi-major axis and the semi-minor axis of the ellipse are 2.5 m and 1.5 m, respectively. The ellipse (the dotted line) is centered at $[4.0, 3.0, 1.5]^{\mathrm{T}}$ m, i.e. the center of the considered area. Starting at the coordinates $[4.0, 4.5, 1.5]^{\mathrm{T}}$ m (the black arrow), the path oscillates sinusoidally in the Z direction and completes the path with three periods. The receiver follows the path clockwise, and at each sample point the orientation of the receiver is chosen such that the frame of the receiver is tangent to the path, more specifically, $\mathbf{R} = \exp\left((\theta_R \mathbf{n}_{R,y})_\times\right) \mathbf{R}_0$, where $\mathbf{R}_0 = [\mathbf{n}_{R,x}, \mathbf{n}_{R,y}, \mathbf{n}_{R,z}]$, $\mathbf{n}_{R,z} = \mathbf{n}_{R,x} \times \mathbf{n}_{R,y}$, $\mathbf{n}_{R,y}$ is the unit tangent vector of the path at the sample point, $\mathbf{n}_{R,x}$ is the unit vector that resides in the XY plane and satisfies $\mathbf{n}_{R,x}^{\mathrm{T}} \mathbf{n}_{R,y} = 0$ and $[\mathbf{n}_{R,z}]_3 > 0$, and θ_R (the roll angle) controls how much $\mathbf{R}_0$ is rotated around $\mathbf{n}_{R,y}$. The frame of the receiver (the column vectors of $\mathbf{R}$) along the path is illustrated in Fig. 5 (shown with $\theta_R = 0°$) by three orthonormal vectors in three different colors. Here we define a parameter $\theta_{\mathbf{r}}$ to specify the sample point, where $\theta_{\mathbf{r}}$ is the traveled angle along the ellipse pattern in the XY plane. In the following, the SNR is defined as SNR $\triangleq \left(\frac{A_R P_t R_p}{2\pi\sigma_w}\right)^2$. To the best of our knowledge, there is no algorithm that simultaneously estimates position and orientation for MLMP-based VLP systems. Therefore, for comparison, we will use as baseline method the algorithm from [20], which estimates the position of the receiver only. In this baseline method, we set the rotation matrix $\hat{\mathbf{R}}$ equal to

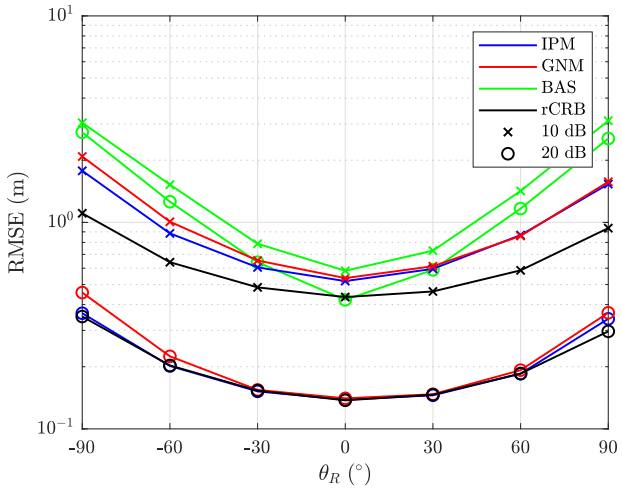

(a) ‘

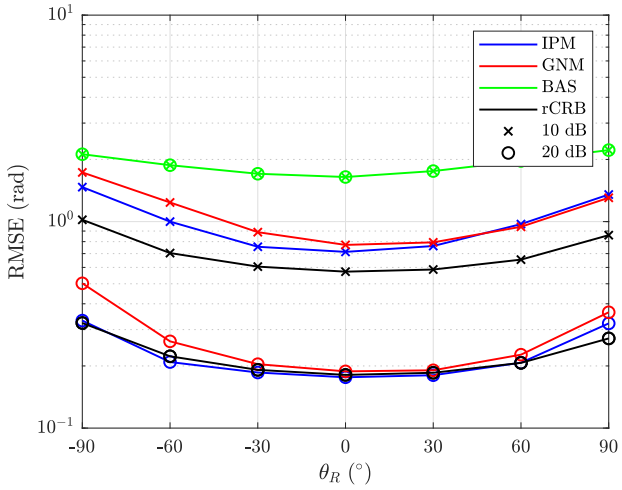

(b)

Fig. 8. RMSE versus θ_R for SNR= 10 dB and SNR= 20 dB. (a) Position estimation errors, (b) Orientation estimation errors.

the identity matrix, i.e., we assume the receiver points straight upwards.

A. Performance of the Estimators

First, we consider the case of a roll angle $\theta_R = 0°$, implying the x-axis of the receiver frame stays horizontal in the system frame. The convergence behavior of the proposed methods is presented in Fig. 6, which gives the average RMSE over the entire path as a function of the number of iterations when SNR $=$ 10 dB and SNR $=$ 20 dB. First, we notice that, as expected, the baseline method (BAS) shows an improving performance as a function of the number of iterations for the position estimation, but a high, constant RMSE for the orientation estimation. This is explained as the baseline method estimates only the position but not the orientation. Because of this limitation, the gap between the RMSE of the baseline method and the proposed CRB is the largest. On the other hand, the proposed algorithms based on the Gauss-Newton method (GNM) and the interior point method (IPM) converge to the CRB for a SNR of 20 dB, and show only a small gap with the CRB for a SNR of 10 dB. Hence, the proposed algorithms outperform the algorithm from [20]. Comparing the convergence rate, we see that the convergence for the orientation is similar for both the GNM and the IPM, whereas for the position estimation, the GNM shows a slower convergence. This is due to the absence of the boundary condition in the GNM, implying outliers can occur where the algorithm returns a position estimate outside the considered area, resulting in large errors that slow down the convergence. In Fig. 7, the RMSE of the estimate of the position and orientation for the proposed estimators are shown as a function of $\theta_{\mathbf{r}}$ for the same SNRs as used in Fig 6. Taking into account that the path we consider has a sinusoidal pattern in the Z direction, there is a relatively larger distance between the receiver and the LED in the valleys of the path. At the same time, since the path has an elliptical pattern in the XY plane, the largest distance between the receiver and the LED occurs at the vertex of the ellipse lying in a valley. Since the channel gain is inversely proportional to the distance between the receiver and the LED, a higher RMSE is expected at those points in the path that have a larger distance between the receiver and the LEDs. This can be observed in Fig. 7, where the performance along the path shows a sinusoid-like pattern with three peaks and valleys appearing in the RMSEs, corresponding to the valleys and peaks in the path. The largest RMSE is obtained around $\theta_{\mathbf{r}} = 90°$, which corresponds to the largest distance point (the vertex in the valley). Comparing the performances for different SNRs, we can see that for SNR $=$ 20 dB, both proposed estimators reach the theoretical bound, while for SNR $=$ 10 dB, the IPM outperforms the GNM. As can be observed, the RMSE of the baseline method for both position and orientation estimation is (approximately) the same for 10 dB and 20 dB SNR. Hence, due to the absence of orientation estimation in the baseline method, the position estimate suffers from a bias. The baseline's RMSE for the orientation is due to the difference between the true orientation, specified by the path, and the reference orientation used in the baseline method, i.e., the identity matrix. When $\theta_{\mathbf{r}}/180° = 3/2$, the true orientation has a rotation matrix equal to the identity matrix, implying the RMSE of the baseline method for the orientation equals zero (see both Fig. 7c and Fig. 7d). As can be seen in Fig 7, the baseline method generally performs worse when the true orientation $\mathbf{R}$ is not the identity matrix. In Fig. 6 and Fig. 7, we observe that at SNR $=$ 10 dB, there is a the gap between the performance of the proposed methods (GNM and IPM) and the CRB. This gap is caused by the threshold phenomenon of the CRB, which will be discussed in the following subsection.

Next, we will investigate the effect of the receiver orientation on the performance. Fig. 8 gives the average RMSE over the entire path as a function of the roll angle θ_R when SNR $=$ 10 dB and SNR $=$ 20 dB. Because all LEDs are attached to the ceiling, the receiver will sense less LEDs when θ_R is increased. This can be observed in Fig. 8, as the RMSE increases when $|\theta_R|$ increases. Further, from the figure, it follows that the performance is worse when $\theta_R < 0$. This can be explained as when $\theta_R < 0$, the receiver is tilted towards the side boundary of the area, implying less

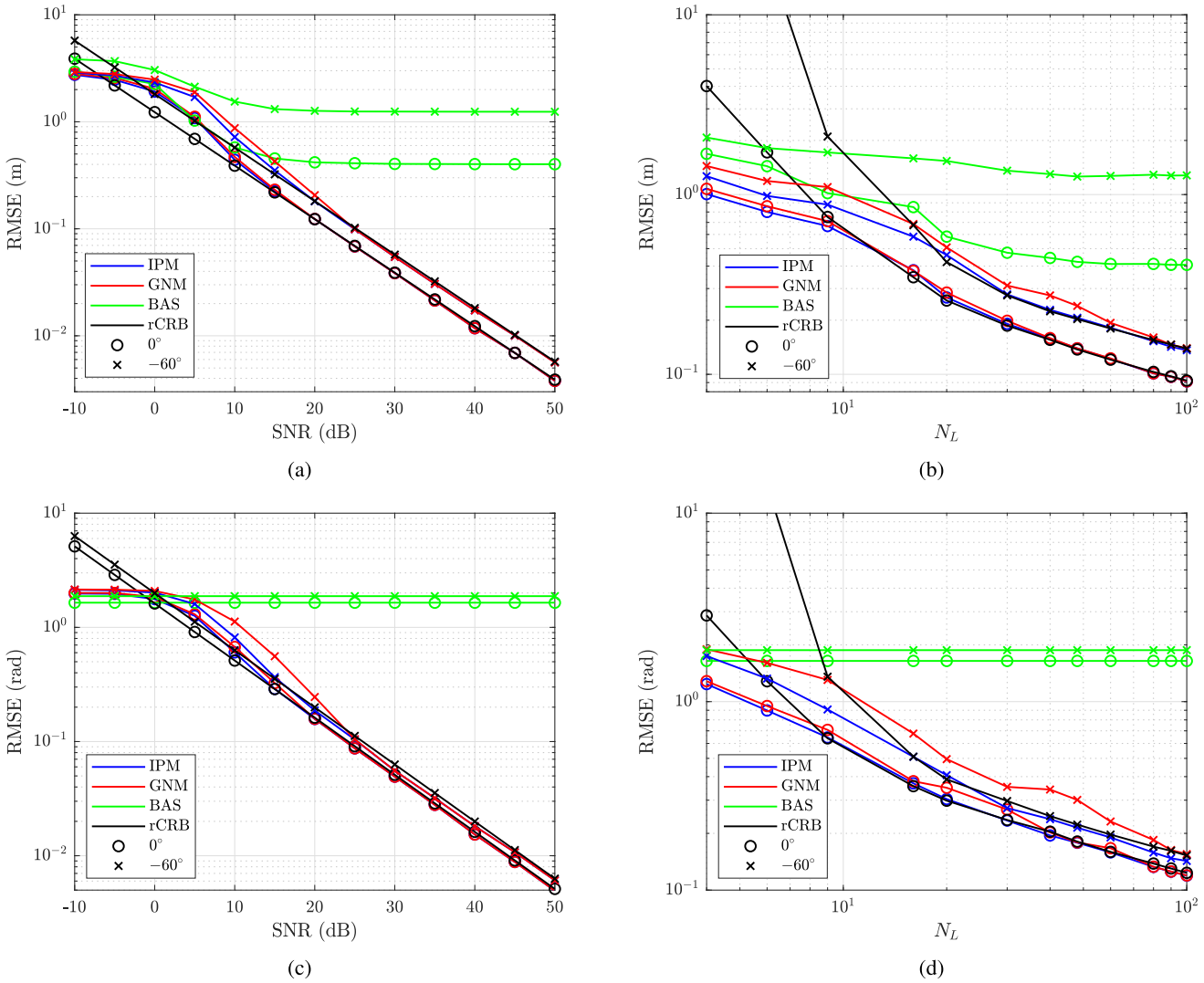

Fig. 9. RMSEs of estimating position and orientation parameters as a function of SNR ((a) position estimation errors and (c) orientation estimation errors when $N_L = 48$) and as a function of the number of LEDs ((b) position estimation errors and (d) orientation estimation errors when SNR $= 20$ dB) for Case 1: $\theta_R = 0°$ and Case 2: $\theta_R = -60°$. Upper row ((a) and (b)) for position estimation errors, bottom row ((b) and (d)) for orientation estimation errors.

LEDs will be visible compared to the case with $\theta_R > 0$. It also can can be seen in Fig. 8 that when the magnitude of θ_R increases, the estimators' performance degrades, and $\theta_R = 0$ corresponds the best performance. Comparing the proposed estimators, we observe that the IPM outperforms the GNM. Especially when $\theta_R < 0$, the GNM fails to converge properly, as the number of LEDs seen by the receiver is too low.

B. Asymptotic Tightness

In this section, to investigate the asymptotic tightness of the theoretical bound, the estimators are simulated for various values of SNR and numbers of LEDs. The configuration is the same as in Fig. 5. In Fig. 9, we show the RMSE averaged over the path for two roll angles (Case 1: $\theta_R = 0°$, Case 2: $\theta_R = -60°$) as a function of the SNR (Fig. 9a and 9c), and as a function of the number N_L of LEDs (Fig. 9b and 9d). As expected, increasing the SNR or N_L leads to a lower RMSE, and we observe an asymptotic tightness of both proposed estimators to the lower bound. Due to the introduced bias, the performance of the baseline method shows an error floor when SNR or N_L is large. At low SNR or low N_L, the RMSE deviates from the CRB. This is explained as for these cases, the bias in the position and orientation estimates becomes non-negligible. Taking into account that the CRB only can serve as a lower bound for unbiased estimators, this implies that, below a threshold for the SNR or N_L, no asymptotic tightness can be reached between the RMSE of the proposed estimators and the CRB.

C. Impact of Location of the Receiver

In this section, we investigate the CRB as a function of the position of the receiver. Considering the setup illustrated in Fig. 5, the CRB for SNR $= 20$ dB is shown in Fig. 10a and Fig. for the XY plane fixed at $z = 1.5$ m, while in Fig. 10b and Fig. 10d the CRB averaged over the XY plane is plot as a function of the height for SNR $= \{20, 30, 40\}$ dB. The spatial sample points are evenly distributed in the area with an

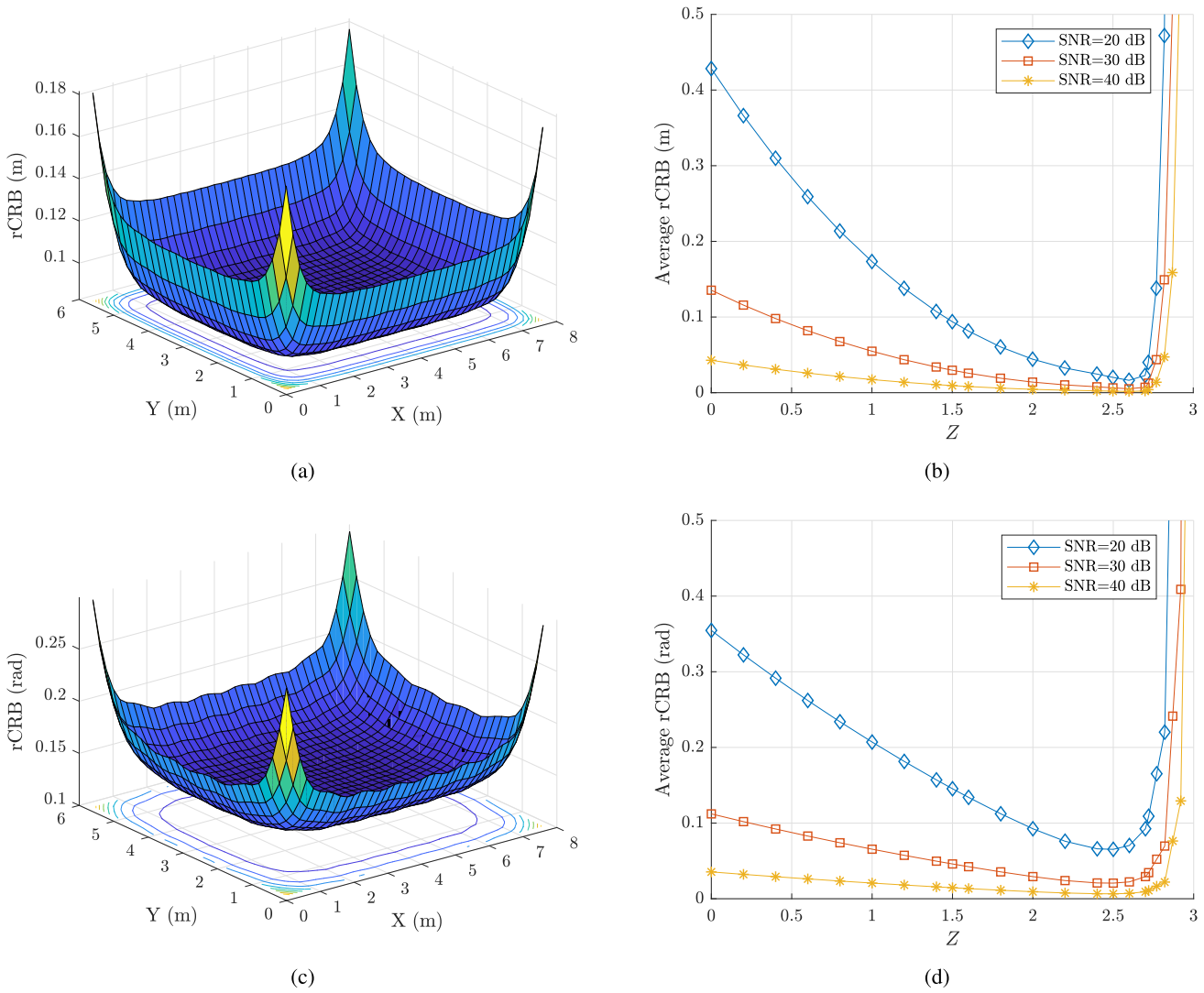

Fig. 10. Averaged CRB as a function of the position of the receiver. (a) The CRB on the position vector and (c) the CRB on the orientation matrix for the XY plane fixed at 1.5 m in z-axis. (b) The CRB on the position vector and (d) the CRB on the orientation matrix as a function of the height.

interval of 0.2 m, and at each sample point, multiple random orientations of the receiver are generated. Considering that in reality the receiver will be placed roughly upwards, the zenith angle of the generated orientation is uniformly distributed within the interval $[-60°, 60°]$. The corresponding random rotation matrix can be generated using the fast algorithm given in [45].

Due to the limited FOV of the receiver, the closer the receiver is to the side boundary of the area, the lesser LEDs it will sense. This explains the inverted dome shape of the CRB in Fig. 10a and Fig. 10c, where the lowest point is obtained near the center of the XY plane, while the largest values locate around the four corners. The limited FOV also explains the results of Fig. 10b and Fig. 10d, where the CRB is shown as a function of the height of the receiver. While the CRB first improves for increasing height, as the distance between the LEDs and the receiver reduces, for larger heights, the CRB degrades again, because the angle between the receiver and the LEDs increases, and the LEDs start to fall outside the FOV of the receiver.

D. Configuration of the Receiver

In this section, we investigate the impact of the diversity angle θ_P, i.e., the tilt angle between the PDs and the centroid of the receiver, on the position and orientation estimation accuracy. By increasing θ_P, we increase the FOV of the receiver, as the receiver array will be able to sense LEDs that are at larger incident angle. However, at the same time, each PD of the receiver will sense less LEDs because of the larger tilt angle, so the diversity of the receiver reduces. To find the optimal configuration, the system setup and the sampling method used in Subsection V-C are considered. As can be seen from the previous analysis, the CRB significantly degrades when the height is larger than 2.5 m, and considering that in many cases, the user's main active area is in the lower middle area, samples with a height larger than 2.5 m are discarded. The CRB on the unified estimation error vector $\mathbf{g}_\epsilon$ is used as an indicator. From the previous results, we found that the CRBs on the position and orientation errors are of the same magnitude. Therefore, we set the scale factor $\xi = 1$. The

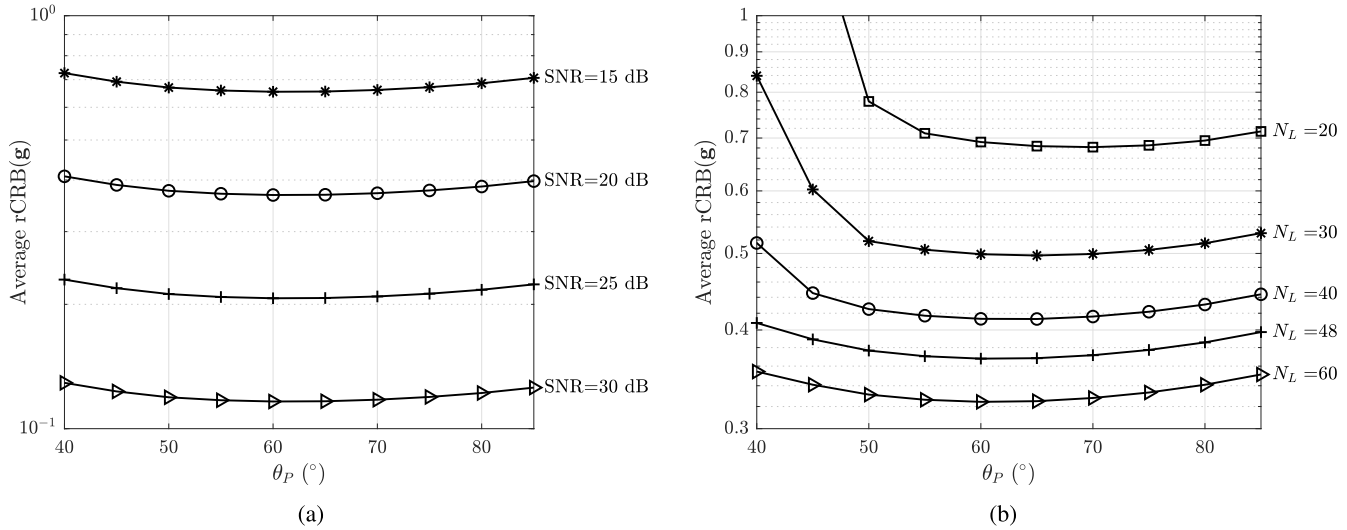

Fig. 11. Averaged CRB as a function of θ_P. (a) CRB for different SNRs (b) CRB for different N_Ls.

spatial averaged CRB is first plotted in Fig. 11a for different SNR and is then plotted in Fig. 11b for different N_L. From Fig. 11a, it follows that the minimum of the CRB is obtained at $\theta_P = 60°$ for all SNR values. However, it can also be observed that the minimum is very broad, indicating that the performance will be rather insensitive to the value of the tilt angle for given SNR. When changing the number N_L of LEDs, we see a larger dependency on θ_P, especially for small values of N_L (see Fig. 11b). When N_P is sufficiently large, again the optimal tilt angle equals $\theta_P = 60°$. However, when $N_L \leq 40$, the performance rapidly degrades when $\theta_P \leq 50°$, and the optimal value of the tilt angle increases. This can be explained as when less LEDs are available, a larger FOV is required to capture more LEDs at the receiver.

VI. Conclusion

In this study, we design two RSS-based simultaneous position and orientation estimation algorithms for a visible light system. Both algorithms exploit the principle of optimization on manifolds, which alleviates the constraints imposed by the restrictions on the rotation matrix, and increases the robustness of estimation. As the proposed algorithms are iterative and need a proper initialization to converge, we propose a coarse estimator that uses the direct linear transformation. To theoretically analyze the proposed estimators, we evaluate the CRB for simultaneous position and orientation estimation. The part of the CRB corresponding to the orientation errors is the intrinsic CRB, and is used to measure errors in the estimated rotation matrix in a physically meaningful way.

The proposed estimators show asymptotic convergence to the CRB, indicating the proposed estimators have excellent performance. Comparing the results of both algorithms before convergence, we show that the interior point method outperforms the Gauss-Newton method, but at the cost of complexity.

Based on the CRB, we also investigated the performance of the simultaneous position and orientation estimation as a function of the position of the receiver and the parameters of the system. Based on these results, we can conclude that the optimal configuration of the receiver consists of PDs that are tilted over $60°$ with respect to the normal of the receiver, to obtain a good trade-off between the FOV and diversity of the receiver.

References

[1] M. Ayyash *et al.*, "Coexistence of WiFi and LiFi toward 5G: Concepts, opportunities, and challenges," *IEEE Commun. Mag.*, vol. 54, no. 2, pp. 64–71, Feb. 2016.

[2] E. Björnson, L. Sanguinetti, H. Wymeersch, J. Hoydis, and T. L. Marzetta, "Massive MIMO is a reality—What is next?: Five promising research directions for antenna arrays," *Digit. Signal Process.*, vol. 94, pp. 3–20, Nov. 2019.

[3] N. Ul Hassan, A. Naeem, M. A. Pasha, T. Jadoon, and C. Yuen, "Indoor positioning using visible LED lights: A survey," *ACM Comput. Surv.*, vol. 48, no. 2, pp. 20:1–20:32, 2015.

[4] A. Jovicic, J. Li, and T. Richardson, "Visible light communication: Opportunities, challenges and the path to market," *IEEE Commun. Mag.*, vol. 51, no. 12, pp. 26–32, Dec. 2013.

[5] Y. Zhuang *et al.*, "A survey of positioning systems using visible LED lights," *IEEE Commun. Surveys Tuts.*, vol. 20, no. 3, pp. 1963–1988, 3rd Quart., 2018.

[6] E.-M. Jeong, S.-K. Han, S.-H. Yang, and H.-S. Kim, "Tilted receiver angle error compensated indoor positioning system based on visible light communication," *Electron. Lett.*, vol. 49, no. 14, pp. 890–892, Jul. 2013.

[7] T. Yuan, Y. Xu, Y. Wang, P. Han, and J. Chen, "A tilt receiver correction method for visible light positioning using machine learning method," *IEEE Photon. J.*, vol. 10, no. 6, pp. 1–12, Dec. 2018.

[8] Q.-L. Li, J.-Y. Wang, T. Huang, and Y. Wang, "Three-dimensional indoor visible light positioning system with a single transmitter and a single tilted receiver," *Opt. Eng.*, vol. 55, pp. 1–7, 2016.

[9] M. F. Keskin, S. Gezici, and O. Arikan, "Direct and two-step positioning in visible light systems," *IEEE Trans. Commun.*, vol. 66, no. 1, pp. 239–254, Jan. 2018.

[10] C. L. Bas, S. Sahuguede, A. Julien-Vergonjanne, A. Behlouli, P. Combeau, and L. Aveneau, "Impact of receiver orientation and position on visible light communication link performance," in *Proc. 4th Int. Workshop Opt. Wireless Commun. (IWOW)*, Sep. 2015, pp. 1–5.

[11] N. Stevens and H. Steendam, "Influence of transmitter and receiver orientation on the channel gain for RSS ranging-based VLP," in *Proc. 11th Int. Symp. Commun. Syst., Netw. Digit. Signal Process. (CSNDSP)*, Jul. 2018, pp. 1–5.

[12] B. Zhou, V. Lau, Q. Chen, and Y. Cao, "Simultaneous positioning and orientating for visible light communications: Algorithm design and performance analysis," *IEEE Trans. Veh. Technol.*, vol. 67, no. 12, pp. 11790–11804, Dec. 2018.

[13] B. Zhou, A. Liu, and V. Lau, "Joint user location and orientation estimation for visible light communication systems with unknown power emission," *IEEE Trans. Wireless Commun.*, vol. 18, no. 11, pp. 5181–5195, Nov. 2019.

[14] W. Xu, J. Wang, H. Shen, H. Zhang, and X. You, "Indoor positioning for multiphotodiode device using visible-light communications," *IEEE Photon. J.*, vol. 8, no. 1, pp. 1–11, Feb. 2016.

[15] S.-H. Yang, E.-M. Jung, and S.-K. Han, "Indoor location estimation based on LED visible light communication using multiple optical receivers," *IEEE Commun. Lett.*, vol. 17, no. 9, pp. 1834–1837, Sep. 2013.

[16] X. Yu, J. Wang, and H. Lu, "Single LED-based indoor positioning system using multiple photodetectors," *IEEE Photon. J.*, vol. 10, no. 6, pp. 1–8, Dec. 2018.

[17] H. Steendam, T. Q. Wang, and J. Armstrong, "Theoretical lower bound for indoor visible light positioning using received signal strength measurements and an aperture-based receiver," *J. Lightw. Technol.*, vol. 35, no. 2, pp. 309–319, Jan. 15, 2017.

[18] T. Q. Wang, C. He, and J. Armstrong, "Performance analysis of aperture-based receivers for MIMO IM/DD visible light communications," *J. Lightw. Technol.*, vol. 35, no. 9, pp. 1513–1523, May 1, 2017.

[19] A. Nuwanpriya, S.-W. Ho, and C. S. Chen, "Indoor MIMO visible light communications: Novel angle diversity receivers for mobile users," *IEEE J. Sel. Areas Commun.*, vol. 33, no. 9, pp. 1780–1792, Sep. 2015.

[20] A. Sahin, Y. S. Eroglu, I. Guvenc, N. Pala, and M. Yuksel, "Hybrid 3-D localization for visible light communication systems," *J. Lightw. Technol.*, vol. 33, no. 22, pp. 4589–4599, Nov. 15, 2015.

[21] M. F. Keskin, E. Gonendik, and S. Gezici, "Improved lower bounds for ranging in synchronous visible light positioning systems," *J. Lightw. Technol.*, vol. 34, no. 23, pp. 5496–5504, Dec. 1, 2016.

[22] M. F. Keskin and S. Gezici, "Comparative theoretical analysis of distance estimation in visible light positioning systems," *J. Lightw. Technol.*, vol. 34, no. 3, pp. 854–865, Feb. 1, 2016.

[23] B. Zhou, A. Liu, and V. Lau, "On the fundamental performance limit of visible light-based positioning," in *Proc. 13th Int. Conf. Signal Process. Commun. Syst. (ICSPCS)*, Dec. 2019.

[24] B. Zhou, A. Liu, and V. Lau, "Performance limits of visible light-based user position and orientation estimation using received signal strength under NLOS propagation," *IEEE Trans. Wireless Commun.*, vol. 18, no. 11, pp. 5227–5241, Nov. 2019.

[25] J. Mäkinen, "Rotation manifold SO(3) and its tangential vectors," *Comput. Mech.*, vol. 42, no. 6, p. 907, May 2008, doi: 10.1007/s00466-008-0293-z.

[26] J. M. Kahn and J. R. Barry, "Wireless infrared communications," *Proc. IEEE*, vol. 85, no. 2, pp. 265–298, Feb. 1997.

[27] H. Steendam, "A 3-D positioning algorithm for AOA-based VLP with an aperture-based receiver," *IEEE J. Sel. Areas Commun.*, vol. 36, no. 1, pp. 23–33, Jan. 2018.

[28] M. Biagi, A. M. Vegni, and T. D. C. Little, "LAT indoor MIMO-VLC—Localize, access and transmit," in *Proc. Int. Workshop Opt. Wireless Commun. (IWOW)*, Oct. 2012, pp. 1–3.

[29] S. Pergoloni, Z. Mohamadi, A. M. Vegni, Z. Ghassemlooy, and M. Biagi, "Metameric indoor localization schemes using visible lights," *J. Lightw. Technol.*, vol. 35, no. 14, pp. 2933–2942, Jul. 15, 2017.

[30] P.-A. Absil, R. Mahony, and R. Sepulchre, *Optimization Algorithms on Matrix Manifolds*. Princeton, NJ, USA: Princeton Univ. Press, 2009.

[31] C. J. Taylor and D. J. Kriegman, "Minimization on the Lie Group SO(3) and related manifolds," Yale Univ., New Haven, CT, USA, Tech. Rep. 9405, 1994.

[32] T. D. Barfoot, *State Estimation for Robotics*. Cambridge, U.K.: Cambridge Univ. Press, 2017.

[33] J. Nocedal and S. Wright, *Numerical Optimization*. Springer, 2006.

[34] R. H. Byrd, G. Liu, and J. Nocedal, "On the local behavior of an interior point method for nonlinear programming," *Numer. Anal.*, vol. 1997, pp. 37–56, 1997.

[35] C. F. Van Loan and G. H. Golub, *Matrix Computations*. Baltimore, MD, USA: Johns Hopkins University Press, 1983.

[36] J. J. Craig, *Introduction to Robotics: Mechanics and Control, 3/E*. New Delhi, India: Pearson Education India, 2009.

[37] S. M. Kay, *Fundamentals of Statistical Signal Processing: Estimation Theory*. Upper Saddle River, NJ, USA: Prentice-Hall, 1993.

[38] S. Bonnabel and A. Barrau, "An intrinsic Cramér-Rao bound on SO(3) for (dynamic) attitude filtering," in *Proc. 54th IEEE Conf. Decis. Control (CDC)*, Dec. 2015, pp. 2158–2163.

[39] Z. Chen, N. Serafimovski, and H. Haas, "Angle diversity for an indoor cellular visible light communication system," in *Proc. IEEE 79th Veh. Technol. Conf. (VTC Spring)*, May 2014, pp. 1–5.

[40] C. Chen, W.-D. Zhong, H. Yang, S. Zhang, and P. Du, "Reduction of SINR fluctuation in indoor multi-cell VLC systems using optimized angle diversity receiver," *J. Lightw. Technol.*, vol. 36, no. 17, pp. 3603–3610, Sep. 1, 2018.

[41] A. Taha Hussein, M. T. Alresheedi, and J. M. H. Elmirghani, "Fast and efficient adaptation techniques for visible light communication systems," *IEEE/OSA J. Opt. Commun. Netw.*, vol. 8, no. 6, pp. 382–397, Jun. 2016.

[42] P. Sturm, "Algorithms for plane-based pose estimation," in *Proc. IEEE Conf. Comput. Vis. Pattern Recognit. CVPR*, Jun. 2000, pp. 706–711.

[43] R. Hartley and A. Zisserman, *Multiple View Geometry in Computer Vision*. Cambridge, U.K.: Cambridge Univ. Press, 2003.

[44] Z. Ghassemlooy, W. Popoola, and S. Rajbhandari, *Optical Wireless Communications: System and Channel Modelling With Matlab*. Boca Raton, FL, USA: CRC Press, 2019.

[45] J. Arvo, "Fast random rotation matrices," in *Graphics Gems III (IBM Version)*. Amsterdam, The Netherlands: Elsevier, 1992, pp. 117–120.

Shengqiang Shen received the B.S. degree in information engineering from the China University of Mining and Technology, Xuzhou, China, in 2013. He is currently pursuing the Ph.D. degree with Digital Communications Research Group, Department of Telecommunications and Information Processing, Ghent University, Belgium. His research interests include visible light positioning and wireless communication.

Shiyin Li received the Ph.D. degree in information and communication engineering from the China University of Mining and Technology, Xuzhou, China, in 2010. Since 2010, he has been a Professor with the School of Information and Control Engineering, China University of Mining and Technology. He is currently the Head of the Department of Information Engineering. His research interests include wireless communication and network congestion control.

Heidi Steendam (Senior Member, IEEE) received the M.Sc. degree in electrical engineering and the Ph.D. degree in applied sciences from Ghent University, Gent, Belgium, in 1995 and 2000, respectively.

Since September 1995, she has been with Digital Communications (DIGCOM) Research Group, Department of Telecommunications and Information Processing (TELIN), Faculty of Engineering, Ghent University, first in the framework of various research projects, and since October 2002 as has been a Professor of digital communications. She was a Visiting Professor with Monash University in 2015, and in 2019 with ESPOL. Her main research interests are in statistical communication theory, carrier and symbol synchronization, bandwidth-efficient modulation and coding, cognitive radio and cooperative networks, positioning, and visible light communication. She is the author of more than 150 scientific articles in international journals and conference proceedings, for which several best paper awards were received. Since 2002, she has been an executive Committee Member of the IEEE Communications and Vehicular Technology Society Joint Chapter, Benelux Section, since 2012 the Vice Chair and since 2017 the Chair. She was active in various international conferences as Technical Program Committee Chair/Member and the Session Chair. In 2004 and 2011, she was the Conference Chair of the IEEE Symposium on Communications and Vehicular Technology in the Benelux. From 2012 to 2017, she was an Associate Editor of the IEEE TRANSACTIONS ON COMMUNICATIONS and the *EURASIP Journal on Wireless Communications and Networking*.